

May 11, 2022

A first survey of spinning eccentric black hole mergers: numerical relativity simulations, hybrid waveforms, and parameter estimation

Antoni Ramos-Buades,¹ Sascha Husa,¹ Geraint Pratten,^{1,2} Héctor Estellés,¹
Cecilio García-Quirós,¹ Maite Mateu,¹ Marta Colleoni,¹ and Rafel Jaume¹

¹*Departament de Física, Universitat de les Illes Balears, IAC3 – IEEC, Crta. Valldemossa km 7.5, E-07122 Palma, Spain*

²*School of Physics and Astronomy and Institute for Gravitational Wave Astronomy, University of Birmingham, Edgbaston, Birmingham, B15 9TT, United Kingdom*

We analyze a new numerical relativity data set of spinning but non-precessing binary black holes on eccentric orbits, with eccentricities from approximately 0.1 to 0.5. Spinning black holes with dimensionless spins of up to 0.75 are included at mass ratios $q = m_1/m_2 = (1, 2)$, and further non-spinning binaries at mass ratios $q = (1.5, 3, 4)$. Comparison of the final mass and spin of these simulations with non-eccentric data extends previous results in the literature on circularisation of eccentric binaries to the spinning case. For the $(l, m) = (2, 2)$ spherical harmonic mode we construct eccentric hybrid waveforms that connect the numerical relativity data to a post-Newtonian description for the inspiral, and we discuss the limitations in the current knowledge of post-Newtonian theory which complicate the generation of eccentric hybrid waveforms. We also perform a Bayesian parameter estimation study, quantifying the parameter biases introduced when using quasicircular waveform models to estimate the parameters of highly eccentric binary systems. We find that aligned-spin quasicircular models with higher order modes produce lower biases in certain parameters, like the mass ratio and the luminosity distance, than aligned-spin quasicircular models with only the $(l, m) = (2, \pm 2)$ modes and precessing models.

PACS numbers: 04.25.Dg, 04.25.Nx, 04.30.Db, 04.30.Tv

I. INTRODUCTION

The detections of gravitational wave signals [1–8] have been found consistent with models of the waveform emitted from the merger of compact objects under the assumption of quasi-circularity of the binary’s orbit prior to the merger. The assumption of quasicircularity motivated by the efficient circularization of binaries as a consequence of the emission of gravitational waves [9, 10] simplifies significantly the complexity of the signal and has accelerated the development of inspiral-merger-ringdown (IMR) waveform models: several mature IMR models for quasi-circular coalescences, i.e. neglecting eccentricity, are now publicly available [11–20], and are being used to search and infer the parameters of observed binary black hole systems [7].

Recently, population synthesis studies [21–24] have shown that active galactic nuclei and globular clusters can host a population of moderate and highly eccentric binaries emitting in the frequency band of ground-based detectors. Therefore, the increase in sensitivity of the detectors will increase the likelihood to detect binary systems with non-negligible eccentricities. The modelling of the gravitational waveforms from eccentric black-hole binaries complicates due to the addition of a new timescale to the binary problem, the periastron precession [25]. This new timescale induces oscillations in the waveforms due to the asymmetric emission of gravitational radiation between the apastron and periastron passages.

The orbits of eccentric black-hole binaries are typically described using the Quasi-Keplerian (QK) parametrization [26], which is currently known up to 3 Post-Newtonian (PN) order [27]. This parametrization has been proven a key element to develop inspiral PN waveforms [28–30]. The generation

of IMR eccentric models relies on the connection of an eccentric PN inspiral with a circular merger [31, 32]. Alternatively, one can substitute the PN waveform by one produced within the Effective One Body (EOB) formalism describing an eccentric inspiral [33, 34]. Some eccentric IMR waveform models show good agreement with numerical waveforms up to $e \sim 0.2$ for non-spinning configurations [31]. The extension of these models to the spinning case is challenging due to their construction based on the QK parametrisation, whose extension to include spins is not known yet.

In this paper we present the input data and some key tools required for the development of an IMR eccentric waveform model calibrated to eccentric hybrid PN-NR waveforms. In Sec. II we first present our Numerical Relativity (NR) catalog of non-spinning and spinning eccentric binaries, computed with the private BAM code [35] and the open source Einstein-Toolkit code [36]. This includes a discussion of our procedure to specify the initial parameters of the eccentric simulations in subsection II B, a study of the remnant quantities in Sec. II C, and a new method to measure the eccentricity of NR waveforms with arbitrarily high eccentricity in Sec. II D. We find that the final spin and mass are consistent within the error estimates with the quasicircular case, which extends the study in [37] to the eccentric spinning case. We hybridize the dominant gravitational waveform mode $(2, 2)$ between numerical relativity and post-Newtonian waveforms in Sec. III. This will provide the input data for future work on constructing waveform models that contain the inspiral, merger and ringdown, and allows us to perform injections into detector noise which contain a long inspiral phase. In Sec. IV we use such injections of hybrid waveforms, as well as of pure numerical relativity waveforms, to study the parameter biases introduced

when using quasi-circular waveform models to estimate the parameters of highly eccentric spinning systems. Unless explicitly noted, we are working in geometric units $G = c = 1$. To simplify expressions we will also set the total mass of the system $M = 1$ in Secs. II and III. We define the mass ratio $q = m_1/m_2$ with the choice $m_1 > m_2$, so that $q > 1$. We also introduce the symmetric mass ratio $\eta = q/(1+q)^2$, and we will denote the black hole's dimensionless spin vectors by $\vec{\chi}_i = \vec{S}_i/m_i^2$, for $i = 1, 2$.

II. NUMERICAL RELATIVITY DATA SET

A. Overview

We present a catalog of 60 eccentric NR simulations performed with the private BAM code [35] and the public EinsteinToolkit (ET) [36] with the multipatch Llama thorn [38]. The numerical setup of both codes is the same as in [39]. Most of the simulations are run with the EinsteinToolkit with the multipatch Llama thorn due to its ability to extract the waves at larger extraction radii. The different simulations and their initial conditions are described in Table IV of Appendix A. In Figure 1 we show our choices of mass ratio q , initial eccentricity e_0 , and effective spin parameter, $\chi_{\text{eff}} = (m_1\chi_{1,z} + m_2\chi_{2,z})/(m_1 + m_2)$. We have also added 20 public eccentric SXS simulations presented in [32].

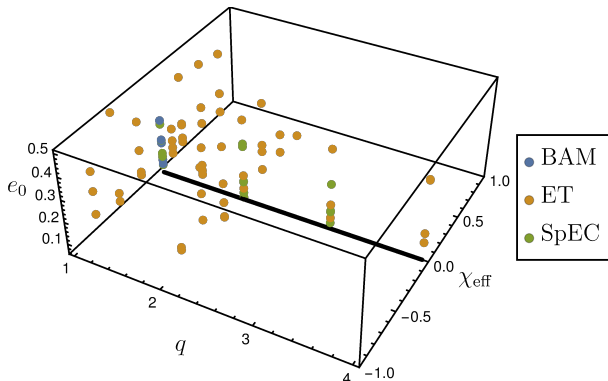


Figure 1: Initial eccentricity e_0 , mass ratio q and effective spin parameter $\chi_{\text{eff}} = (m_1\chi_{1,z} + m_2\chi_{2,z})/(m_1 + m_2)$ for the Numerical Relativity simulations generated with the BAM, EinsteinToolkit and SpEc [40] codes. The thick black line represents the cases with $\chi_{\text{eff}} = 0$.

B. Initial parameters of eccentric NR simulations

We use conformally flat Bowen-York initial data [41] in the center of mass frame, where the free parameters are the spins and masses of the two black holes, the separation, and the momentum of one of the two black holes (the momentum of the second black hole is then equal in magnitude but opposite in direction). We first choose the masses and spins as displayed in Fig. 1. In order to be able to construct hybrid

waveforms, the minimal separation, i.e. the separation at periastron, has to be large enough such that the PN approximation is still roughly valid. We then use a simple PN approximation as discussed below to compute the apastron separation required to achieve a chosen value of the eccentricity, and a further PN approximation to compute the appropriate value of the momentum corresponding to this value of the eccentricity. Due to the simplicity, i.e. low order, of the PN approximations used, neither the periastron separation, nor the measured eccentricity will exactly coincide with the specified values. In this study we will chose our initial choice for the approximate periastron separation as $r_{\text{min}} = 9M$. We start our simulations at the apastron, where the PN approximation we use to specify the initial momentum, and the agreement with the PN data we use for hybridization, will be more accurate than during other points of the orbit.

Larger choices of eccentricity for the same configuration of masses and spins thus lead to larger merger time and number of orbits, as one can see in Table IV of Appendix A. For instance, focusing on simulations with IDs 34, 35 and 36 one observes an increase in the merger time when increasing the initial eccentricity. This increase in merger time also implies an increase in the computational cost of the simulation.

Using the QK parametrization at Newtonian order one can relate the initial minimum and maximum separations by

$$r_{\text{min}} = r_{\text{max}} \frac{1-e}{1+e}. \quad (2.1)$$

As stated above, for our simulations we choose $r_{\text{min}} = 9M$ such that the PN approximation is still roughly valid. Then for $e_0 = 0.1, 0.2, 0.5$ Eq. (2.1) implies that $r_{\text{max}} = 11, 13.5, 27$, respectively. These values of r_{max} have been used as references to specify the initial separations of the simulations in Table IV.

In order to produce initial data for a desired eccentricity we then make use of Eq. (3.25) of [39] to perturb the initial tangential momentum of the puncture by a factor λ_t from its quasicircular value. The expression for λ_t in terms of the eccentricity at 1PN order is

$$\lambda_t(r, e, \text{sign}) = 1 + \frac{e}{2} \times \text{sign} \times \left[1 - \frac{1}{r}(\eta + 2) \right], \quad (2.2)$$

where η is the symmetric mass ratio, r is the orbital separation and $\text{sign} = \pm 1$ depends on the initial phase of the eccentricity estimator [39]. We refer the reader to Sec. III D of [39] for an explicit derivation of Eq. (2.2). Taking Eq. (2.2) we compute the correction factor applied to the momentum as the mean between the inverse of the expression with the plus sign plus the expression with the minus sign,

$$\bar{\lambda}_t^0 = \frac{1}{2} \left[\lambda_t(r, e, +1)^{-1} + \lambda_t(r, e, -1) \right] = \frac{8r^2 - e^2(\eta - r + 2)^2}{4r(e(-\eta + r - 2) + 2r)}. \quad (2.3)$$

We use the combination of factors in Eq. (2.3) because we have experimentally tested that it works more accurately than just specifying a value of $\lambda_t(r, e, \text{sign})$ with a given sign. In

Table IV one can compare the value of the desired initial eccentricity, written in the tags of the simulations, with the measured initial eccentricity, given in the last column of Table IV. One observes that the use of this particular combination of correction factors produces simulations with an initial eccentricity with a difference of less than 10% with respect to the desired one for non-spinning cases at low eccentricities of the order of 0.1. However, when spins are present or the eccentricities are higher, the inaccuracy of the formula becomes manifest, with differences of the order of 20–30%, this is due to the fact that Eq. (2.2) was derived assuming a non-spinning binary in the low eccentric limit. Additionally, one can check in Table IV that the measured eccentricity of the cases with positive spins is closer to the one of the tags than those cases with negative spins because in Eq. (2.2) the radiation reaction effects, which are more significant for negative spins, were also not taken into account.

C. Final state of spinning eccentric systems

We compare the final state of the eccentric NR simulations with the predicted final mass and final spin of the QC NR fits [42] as an indicator of circularisation of the coalescence process as the binary merges. This is basically an extension of [37] to the eccentric spinning case with more moderate values of the eccentricity, but with longer NR evolutions.

The final mass and final spin of the simulations are computed using the apparent horizon (AH) of the remnant black hole and are shown in Table IV. The magnitude S of the angular momentum of the final black hole can be computed from the integral

$$S = \frac{1}{8\pi} \oint_{\text{AH}} K_{ij} n^i \phi^j dA, \quad (2.4)$$

see the discussion in [43, 44]. Here for the BAM code [45] the vector ϕ^j is a coordinate-based approximation to the (approximate) axial Killing vector of the black hole horizon as in [43], and for the Einstein Toolkit code the `QuasiLocalMeasures` thorn is used, which constructs an approximate Killing vector with rotational symmetry around the spin axis as in [46, 47]. The vector n^i is a spacelike unit normal to the horizon surface and K_{ij} is the extrinsic curvature. The final mass can be computed from the Christodoulou formula in terms of the BH angular momentum and AH area A as

$$M_f = \sqrt{M_{irr}^2 + \frac{S^2}{4M_{irr}^2}}, \quad M_{irr} = \sqrt{\frac{A}{16\pi}}. \quad (2.5)$$

where M_{irr} is the irreducible mass. The dimensionless final spin can then be computed as $\chi_f = S/M_f^2$.

In Fig. 2 we have computed the absolute and relative errors between the eccentric simulations and the quasicircular NR final mass and final spin fitting formulas [42],

$$\Delta X = \left[\frac{X^{NR}}{X^{QC}} - 1 \right] \times 100, \quad X = M_f \text{ or } \chi_f. \quad (2.6)$$

The results in Fig. 2 show that the differences in the final spin are generally higher than for the final mass. However, the differences with respect to the quasicircular fitting values are as high as $\sim 1\%$ which is entirely consistent with numerical errors and gauge artifacts in the apparent horizon surfaces and inaccuracies in the fits. Hence, we can conclude that within the current knowledge of systematic errors (compare [42]), the final state of the eccentric simulations up to the values of eccentricity studied here, is consistent with the quasicircular values. Identifying small physical deviations between the quasicircular and eccentric final states will require numerical simulations with improved error estimates.

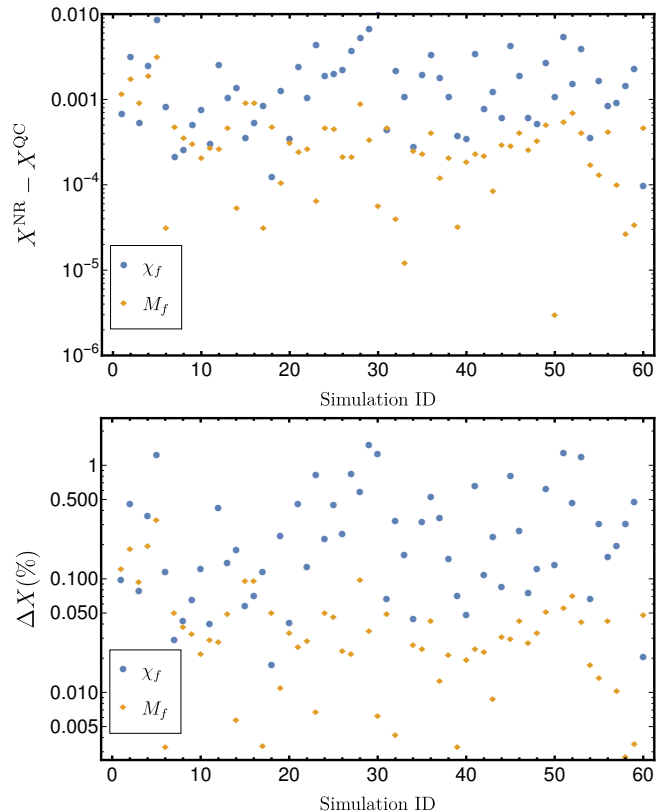


Figure 2: In the top panel the difference between the final mass and spin of the simulations and the QC NR fits as a function of the ID of the simulations in Table IV. In the bottom plot the absolute relative error for the phase and amplitude, $\Delta X = (X^{NR}/X^{QC} - 1) \times 100$ for $X = M_f, \chi_f$, relative error of the final mass and final spin of the simulations against the QC NR fits as a function of the ID of the simulations in Table IV.

D. Measuring the eccentricity of highly eccentric systems

This subsection aims to extend the discussion on the measurement of the eccentricity in NR presented in [39] to highly eccentric systems. An eccentricity parameter is chosen to describe the non-circularity of orbits, such that for bound orbits its value ranges between 0 and 1, corresponding to circular and extremely elliptical configurations, respectively. Such an

eccentricity can only be defined naturally in Newtonian gravity, whereas in general relativity the eccentricity is a gauge dependent quantity. In order to measure the eccentricity in NR data one defines quantities known as eccentricity estimators, which estimate the eccentricity from the relative oscillations of a certain combination of dynamical quantities such as the orbital separation or orbital frequency, or wave quantities like the amplitude or frequency of the $(l, m) = (2, 2)$ mode. All these different estimators are usually defined such that they agree in the Newtonian limit and in the low eccentricity limit.

In [39], where we studied the reduction of residual eccentricity in initial data sets, we choose our eccentricity estimator based on the orbital frequency as

$$e_{\Omega}(t) = \frac{\Omega(t) - \Omega(e = 0)}{2\Omega(e = 0)}, \quad (2.7)$$

where $\Omega(t)$ is the orbital frequency of the simulation and $\Omega(e = 0)$ is the orbital frequency in the quasicircular limit. This eccentricity estimator is largely used to measure the residual eccentricity of NR simulations of quasicircular black-hole binaries. In [39], we argue that the procedure shown there to measure the eccentricity is limited to values as high as $e \sim 0.1$ due to the lack of an accurate ansatz to fit the higher order contributions beyond the sinusoidal contribution. While the lack of an ansatz for high eccentricities is a clear limitation, the use of (2.7) biases the eccentricity measurement due to its reliance on a non-eccentric fit of the orbital frequency and due to the fact that Eq. (2.7) for high eccentricities does not reduce to the common definition of eccentricity in the Newtonian limit.

Therefore, we decide to change to another estimator [48], constructed also from the orbital frequency,

$$e_{\omega}(t) = \frac{\omega_p^{1/2} - \omega_a^{1/2}}{\omega_p^{1/2} + \omega_a^{1/2}}, \quad (2.8)$$

where ω_a, ω_p are the orbital frequency at apastron and periastron, respectively. The eccentricity estimator in (2.8) does not depend on any non-eccentric fit of the orbital frequency. Furthermore, as shown in Appendix B the eccentricity estimator from (2.7) in the Newtonian limit at high eccentricities does not reduce to the eccentricity parameter and it is not normalized, while the eccentricity estimator from (2.8) fulfills all these conditions.

We measure the eccentricity from the maxima and minima of the orbital frequency. Additionally, we produce an interpolated function from the maxima, ω_p , and the minima ω_a , and substitute them into Eq. (2.8), so that one can estimate the evolution of the eccentricity from those points. The new procedure to measure the eccentricity is shown in Fig. 3, where the time evolution of the orbital frequency, the interpolated functions of the maxima and minima of the orbital frequency and the eccentricity are shown for the configuration with ID 60 from Table IV. As expected the eccentricity is a monotonically decaying function, whose value at $t = 200M$, after the burst of junk radiation, is $e_{\omega} = 0.415 \pm 0.005$. The error in the eccentricity, δe_{ω} , is computed using error propagation: from

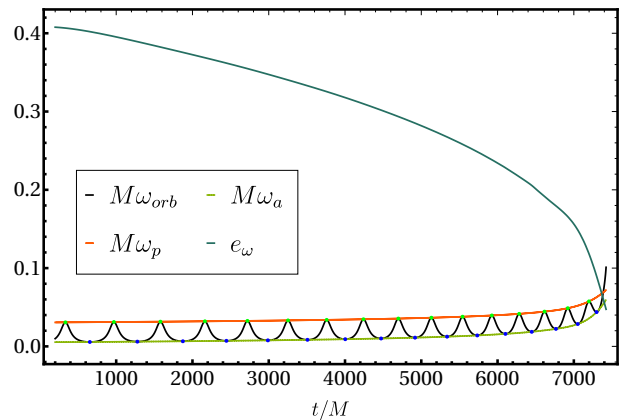


Figure 3: Time evolution of the orbital frequency, $M\omega_{orb}$, the orbital frequency at apastron, $M\omega_a$, the orbital frequency at periastron $M\omega_p$ and the eccentricity estimator, e_{ω} , defined in Eq. (2.8).

Eq. (2.8) we obtain

$$\delta e_{\omega} = \frac{\delta\omega}{(\omega_a^{1/2} + \omega_p^{1/2})^2} \left[\frac{\omega_a^{1/2}}{\omega_p^{1/2}} + \frac{\omega_p^{1/2}}{\omega_a^{1/2}} \right], \quad (2.9)$$

where we have assumed $\delta\omega_a = \delta\omega_p = \delta\omega$. Motivated by the results of the error in the convergence analysis of the orbital frequency in [49] we have taken as a conservative estimate for $\delta\omega = 0.0001$.

The main drawback of this method is that when the simulations are so short that there is only one minimum and one maximum it becomes inefficient and inaccurate. Furthermore, one could choose the frequency of the $(l, m) = (2, 2)$ mode and compute the orbital frequency as $\omega_{orb} \approx \omega_{22}/2$, and employ the same method as discussed in this section. Nevertheless, as pointed out in [50] the usage of the orbital frequency from the $(2, 2)$ mode requires additional post-processing of the data due to the presence of high frequency noise when taking a time derivative of the phase of the $(2, 2)$ mode. As a conclusion, if one has long enough highly eccentric simulations, the method introduced in this section allows one to measure the eccentricity as a monotonically decaying function for the whole inspiral, which is a key tool to be used to construct a time domain eccentric waveform model.

III. HYBRIDIZATION OF ECCENTRIC WAVEFORMS

In the eccentric case the hybridization of the PN-NR waveforms is a challenging problem. The higher the eccentricity the stronger is the interaction between the binary components at each periastron passage, which can break the post-Newtonian, weak-field and low velocity, approximation and generate a secular dephasing between both waveforms. Moreover, the lack of a general description in PN theory of eccentric black-hole binary systems poses the main difficulty. Therefore, we briefly review the status of the PN theory for eccentric systems in Sec. III A. In Sec. III B we show an ex-

ample of our procedure to hybridize eccentric PN-NR waveforms.

A. Review of eccentric post-Newtonian theory

As far as the authors know by the time of writing this communication, the orbital averaged gravitational wave energy flux for eccentric binaries is known up to 3PN order [51] using the 3PN QK parametrization [27]. Our strategy consists in evolving the 3.5PN Hamilton's equations of motion in ADMTT gauge for a point particle binary,

$$\frac{d\mathbf{X}}{dt} = \frac{\partial\mathcal{H}}{\partial\mathbf{P}}, \quad \frac{d\mathbf{P}}{dt} = -\frac{\partial\mathcal{H}}{\partial\mathbf{X}} + \mathbf{F}, \quad \frac{d\mathbf{S}_i}{dt} = \frac{\partial\mathcal{H}}{\partial\mathbf{S}_i} \times \mathbf{S}_i, \quad i = 1, 2. \quad (3.1)$$

with \mathbf{X}, \mathbf{P} and \mathbf{S}_i the position, momentum and spin vectors in the center-of-mass frame, \mathcal{H} the Hamiltonian described in Sec. II of [39] and \mathbf{F} the radiation reaction force described in [52] enhanced with the eccentric contribution to the energy flux from [51]. The eccentric term in the flux is expressed in the QK parametrization and depends only on the orbital frequency ω , which is computed while evolving the system, and the eccentricity e_t , for which we use its 3PN expression in terms of the orbital energy and the angular momentum of the system, which are variables computed at each time step.

The solution of the PN point particle equations, Eqs. (3.1), can be used to compute the gravitational radiation emitted by the system. Here, the lack of general PN expressions for the waveforms of point particles evolving on quasi-elliptical orbits sets a strong limitation. The instantaneous terms of the waveform multipoles are known up to 3PN order for general non-spinning systems with arbitrary eccentricity [53]. Recently, the complete description of the 3PN non-spinning multipoles has been computed including tail and tail-of-tails terms within the QK parametrization for low eccentricities [54]. At this point only using the 3PN instantaneous terms [53] introduces more error than the quadrupole order, due to the missing tail and tail-of-tails terms that enter at 1.5PN, 2.5PN and 3PN orders, respectively. Additionally, the translation of the generic solution we obtain from solving Eqs. (3.1) to the QK form of the waveform modes in [54] is more involved due to the fact that they split the dynamical variables into a secular and oscillatory part. Therefore, we will restrict here to the quadrupole formula to generate the $(l, m) = (2, 2)$ mode and leave for future work the generation of full 3PN waveforms, which will additionally allow us to construct multimode eccentric hybrids.

B. Hybridization example

The hybridization of PN and NR waveforms consists in determining the time shift and phase offset which minimizes the difference between both waveforms in a certain time window. This hybridization procedure is well-established in the quasi-circular case [55–59]. The time shift is usually computed by maximizing a suitable quantity that measures disagreement of

the two waveforms, such as an overlap integral [58, 59], or the deviation between phase or frequency of the $(2, 2)$ mode [55]. However, in the eccentric case the calculation of the time shift requires alignment of the peaks due to eccentricity of both waveforms in the hybridization window. This alignment is complicated to obtain with the phase because the peaks corresponding to each periastron passage are not very pronounced and they are difficult to estimate. One could use the frequency of the $(2, 2)$ mode. However, it is a quantity obtained from a time derivative of the phase, which for NR waveforms tends to be noisy. As a consequence, for simplicity we use the amplitude of the $(2, 2)$ mode to determine the time shift of the waveform because it is a clean quantity with clearly defined peaks.

As an example, we take the NR simulation with ID 60 of Table IV, which is a mass ratio $q = 4$ non-spinning configuration with an initial eccentricity of $e_\omega^0 = 0.415 \pm 0.005$ and initial orbital separation at apastron $D_0 = 27.5M$. We take the initial conditions of the NR simulation defined by the initial position vector, momenta and dimensionless spin vectors: $\mathbf{v}_0 = \{\mathbf{X}, \mathbf{P}, \mathbf{S}_1, \mathbf{S}_2\}_0$. The fact that PN and NR coordinates for the initial data agree up to 1.5PN order [60–62] makes this identification a good approximation, although the missing higher PN orders in the dynamics, but especially in the quadrupole formula we use for the emitted waves, can produce discrepancies between the NR and PN waveforms of the order of 10% or even higher. In order to leverage these differences we decide to modify the initial condition vector of the PN evolution by modifying the initial separation by a δr such that the difference in the amplitude of the Newman-Penrose scalar, ψ_4 , for the $(2, 2)$ mode between PN and NR is minimal. In our example we obtained $\delta r = 0.08$. The outcome of such a calculation can be observed in the top panel of Fig. 4, where the time domain amplitude of the PN and NR waveforms are shown. The procedure is also applied to eccentric aligned-spin configurations. We find that initial highly eccentric configurations require larger δr than low eccentric ones, and that the hybridization errors for high negative spins, where radiation reaction plays a dominant role, are one order of magnitude higher than for non-spinning or low spins due to the lack of expressions for PN spinning eccentric waveforms.

The procedure to construct the hybrid waveform is similar to the one presented in [55]. We first choose the matching region to be after the junk radiation burst, in our particular case we take $t/M \in (275, 375)$. This choice of a short hybridization window is due to the lack of an accurate PN waveform which matches the NR one for long cycles. Then, we have to compute the time shift, τ , and phase offset, φ_0 , which reduce the difference between the PN and NR waveforms in the matching window,

$$h^{PN}(t) = e^{i\varphi_0} h^{NR}(t + \tau). \quad (3.2)$$

In order to align the waveforms in time we choose τ such that it minimizes the amplitude difference along the matching window. For the phase offset we decide to align the phases at the beginning of the the window, $\varphi_0 = \phi^{NR}(t_0 - \tau) - \phi^{PN}(t_0)$, where t_0 is the initial time of the window. Once τ and φ_0 are calculated the hybrid waveform is constructed as a piecewise

function

$$h^{hyb}(t) = \begin{cases} e^{i\varphi_0} h^{PN}(t + \tau) & \text{if } t < t_1 \\ w^-(t)e^{i\varphi_0} h^{PN}(t + \tau) + w^+(t)h^{NR}(t) & \text{if } t_1 < t < t_2 \\ h^{NR}(t) & \text{if } t > t_2 \end{cases} \quad (3.3)$$

where $t_1 = 275M$ and $t_2 = 375M$. The functions $w^\pm(t)$ denote the blending functions defined in the interval $[t_1, t_2]$ that monotonically go from 0 to 1 and from 1 to 0, respectively,

$$w^+(t)_{[t_1, t_2]} = \frac{t - t_1}{t_2 - t_1}, \quad w^-(t)_{[t_1, t_2]} = 1 - w^+(t). \quad (3.4)$$

The result of the application of such a hybridization procedure can be observed in the bottom panel of Fig. 4, where the absolute value of the relative error between the hybrid and NR amplitude and phase are shown. The quantity ΔX is defined as $\Delta X = (X^{hyb}/X^{NR} - 1) \times 100$ for $X = A_{22}, \phi_{22}$. The errors in the amplitude are larger than the ones in the phase, but they are below the 1% threshold. This is due to fact that the amplitude is more oscillatory and, therefore, more sensitive than the phase to the differences between PN and NR.

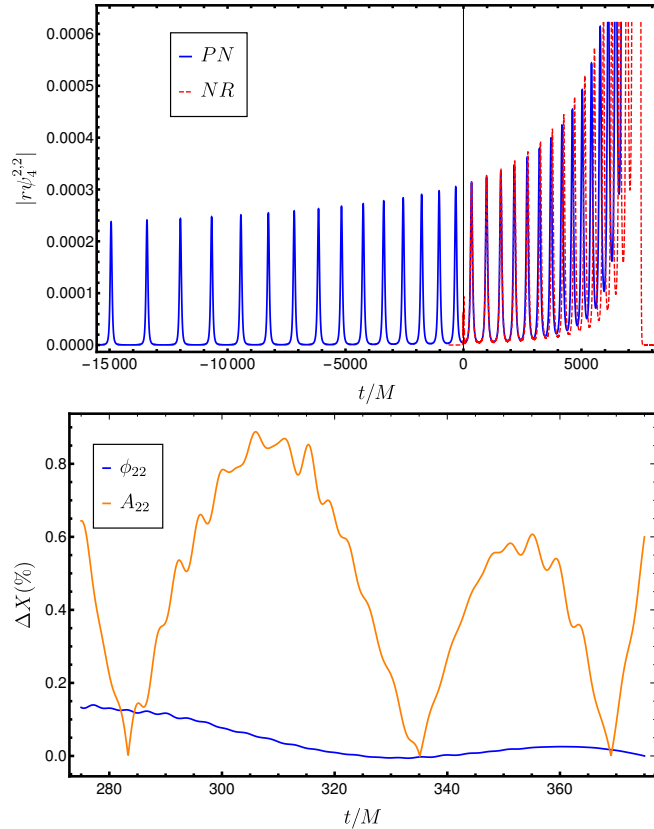


Figure 4: In the top panel the time domain amplitude of the $|r\psi_4^{2,2}|$ mode. The blue thick and the red dashed curves represent the PN and NR waveforms, respectively. In the bottom plot the absolute value of the relative error for the phase and amplitude, $\Delta X = (X^{hyb}/X^{NR} - 1) \times 100$ for $X = \phi_{22}, A_{22}$, of the hybrid against the NR waveform in the matching region is displayed.

Finally, note that the PN waveform used to produce the hybrid is evolved backwards in time from $D_0/M = 27.5$ to

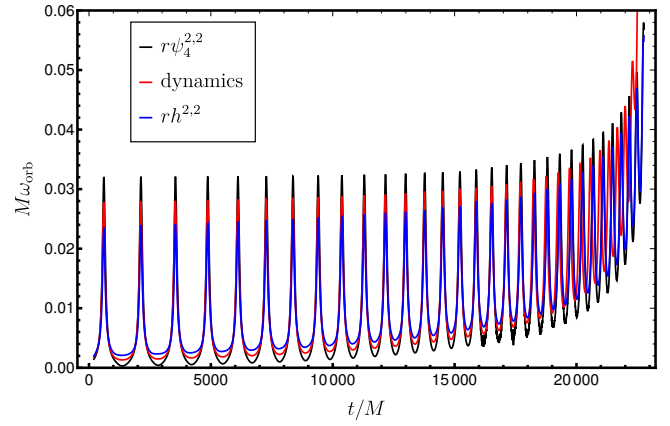


Figure 5: Time evolution of the orbital frequency, $M\omega_{orb}$ computed from the phase of $r\psi_4^{2,2}$, the orbital frequency computed from the dynamics, $\omega = |\frac{\mathbf{v} \times \mathbf{r}}{r^2}|$, and from the phase of the strain $h^{2,2}$.

$D_f/M = 60$. This makes the initial eccentricity to increase with respect to the NR waveform. Next, we explicitly show the systematics affecting the measurement of the initial eccentricity of the hybrid. We display in Fig. 5 the time evolution of the orbital frequency, $\omega_{orb} \approx \dot{\phi}_{22}/2$, computed from the phase of the (2, 2) mode of the Newman-Penrose scalar and the strain computed using Fixed-Frequency Integration (FFI) algorithm [63]. We also compute the orbital frequency from the PN dynamics as,

$$\omega = \left| \frac{\mathbf{v} \times \mathbf{r}}{r^2} \right| \quad (3.5)$$

where $r = |\mathbf{r}|$, and \mathbf{v}, \mathbf{r} are the velocity and the position vectors in the center of mass frame. The curves from Fig. 5 indicate that the orbital frequency computed from ψ_4 and h overestimate and underestimate, respectively, the values of eccentricity with respect to the ones from the dynamics. This is confirmed from the values for the initial eccentricity one obtains from the orbital frequency of the strain, ψ_4 and the dynamics, $e_0^h = 0.55 \pm 0.01$, $e_0^{\psi_4} = 0.84 \pm 0.03$ and $e_0^{dyn} = 0.65 \pm 0.01$, respectively. These three values of eccentricity are measured at the same initial time, $t = 600M$. These results lead to the conclusion that the eccentricity measured from the frequency of the (2, 2) mode is higher for ψ_4 than for h , this can be understood from the fact that $h \approx \int \psi_4 dt'$, therefore, h is a smoother function than ψ_4 . As shown in Fig. 5 this is not a particular result of our procedure to measure the eccentricity, but a general fact which can be reproduced by any method to measure the eccentricity based on the oscillations of the frequency of the (2, 2) mode. Note also that we have decided not to integrate backwards in time too far in the past of the binary due to the inaccuracy of the eccentric PN flux which make the solutions inaccurate for extremely high eccentricities and the inaccuracy of the PN expressions for the waveform which also become more and more inaccurate for high eccentricities.

IV. PARAMETER ESTIMATION WITH ECCENTRIC SIGNALS

In this section we employ the waveforms introduced in Secs. II and III for data analysis studies. First, we analyze the impact of the eccentricity when computing overlaps against quasicircular models. Second, we perform parameter estimation studies injecting eccentric NR and hybrid waveforms into detector noise and compute parameter biases when using quasicircular and inspiral eccentric models available in the LIGO Libraries, LALSUITE [64].

A. Match calculation

A generic black-hole binary evolving in a quasi-elliptical orbit is described by 17 parameters. The intrinsic parameters are the individual masses of the binary m_1, m_2 , the 6 components of the two spin vectors, \vec{S}_1 and \vec{S}_2 , the orbital eccentricity e and the argument of the periastron Ω . The extrinsic parameters describing the sky position of the binary with respect to the detector are: the distance from the detector to the source r , the coalescence time t_c , the inclination ι , the azimuthal angle φ , the right ascension (ϕ), declination (θ) and polarization angle (ψ). All these parameters together describe the strain induced in a detector from a passing gravitational wave [65]

$$h(t, \zeta, \Theta) = [F_+(\theta, \phi, \psi)h_+(t - t_c; \iota, \varphi, \zeta) + F_\times(\theta, \phi, \psi)h_\times(t - t_c; \iota, \varphi, \zeta)]. \quad (4.1)$$

Where $\Theta = \{t_c, r, \theta, \varphi, \alpha, \delta, \psi\}$ is the set of extrinsic parameters and $\zeta = \{m_1, m_2, \vec{S}_1, \vec{S}_2, e, \Omega\}$ are the intrinsic parameters. The detector response is written in terms of the waveform polarizations (h_+, h_\times) which combine to define the complex waveform strain

$$h(t) = h_+ - ih_\times = \sum_{l=2}^{\infty} \sum_{m=-l}^l Y_{lm}^{-2}(\iota, \varphi) h_{lm}(t - t_c; \zeta). \quad (4.2)$$

The comparison between two waveforms is usually quantified by an overlap integral, which is a noise-weighted inner product between the signals [66], and which can be maximised over subsets or all of the parameters of the signal. Given a real-valued detector response, the inner product between the signal, $h_{resp}^S(t)$, and the model, $h_{resp}^M(t)$, is defined as

$$\langle h_{resp}^S | h_{resp}^M \rangle = 4\text{Re} \int_0^{+\infty} \frac{\tilde{h}_{resp}^S(f) \tilde{h}_{resp}^{M*}(f)}{S_n(|f|)} df, \quad (4.3)$$

where \tilde{h} denotes the Fourier transform of h , h^* the complex conjugate of h and $S_n(|f|)$ is the one sided noise Power Spectral Density (PSD) of the detector.

The normalized match optimized over a relative time shift and the initial orbital phase can be written as

$$\mathcal{M}(\iota_S, \varphi_{0_S}) = \max_{t_c, \phi_0} \left[\frac{\langle h_{resp}^S | h_{resp}^M \rangle}{\sqrt{\langle h_{resp}^S | h_{resp}^S \rangle \langle h_{resp}^M | h_{resp}^M \rangle}} \right]. \quad (4.4)$$

The match is close to 1 when the model is able to faithfully reproduce the signal, while values of the match close to 0 indicate large disagreement between the two waveforms. In Eq. (4.4) the match is computed for given values of the angles (ι_S, φ_{0_S}) of the signal and maximizing over phase and time shifts. We will take only the h_{22} mode of the hybrid and PhenomX and we compute single mode mismatches maximized over a time shift, t_0 , and a phase offset, ϕ_0 , as

$$\mathcal{MM} = \max_{t_0, \phi_0} \left[\frac{\langle h_{22}^{\text{hyb}} | h_{22}^{\text{PhX}} \rangle}{\sqrt{\langle h_{22}^{\text{hyb}} | h_{22}^{\text{hyb}} \rangle \langle h_{22}^{\text{PhX}} | h_{22}^{\text{PhX}} \rangle}} \right]. \quad (4.5)$$

To simplify the comparisons we introduce the mismatch, $1 - \mathcal{MM}$. Values of the mismatch close to zero indicate good agreement between the signal and the model, while the higher the mismatch the larger the difference between both waveforms, indicating that the model is not able to accurately represent the signal. Having set the notation for the calculation of the mismatch, we compute the mismatch between the eccentric (2, 2) mode hybrids computed in Sec. III and the quasicircular model PhenomX [18, 19], which is an upgrade of the aligned-spin PhenomD model [12, 67]. We employ the Advanced LIGO 'zero detuned high power' PSD [68] to compute the overlap in Eq. (4.3). The integral of Eq. (4.3) is evaluated between a frequency range of 20 and 2000 Hz. The non-monotonic behavior of the GW frequency of eccentric systems complicates the determination of the frequency range of a signal in the detector band. The ideal case would be the one in which the initial apastron and periastron frequencies are below 20Hz. This would mean that the whole waveform starts before the cutoff frequencies of the detectors and one observes the complete eccentric inspiral of the binary. Another possibility is that both waveforms are above 20 Hz, then the signal is very short and much of the inspiral waveform is lost. Finally, it is also possible that during some part of the waveform the periastron frequencies are above 20 Hz and apastron frequencies are below 20Hz. The latter is typically the case of our hybrid waveforms because of the difficulty to go to the low frequency limit in eccentric systems as explained in Section III B.

In Fig. 6 we show the single mode mismatches between the eccentric hybrids and PhenomX for a range of total mass of the system between $M_T \in \{20, 200\}M_\odot$. As expected, for larger total masses of the system most of the waveform in the frequency band of the detector is in the merger and ringdown parts and the mismatches are even below the 3% threshold. This is consistent with the results obtained in Sec. II C, which show the agreement for the final state between the eccentric simulations and the quasicircular fits. However, the lower the total mass the higher the mismatch, this is due to the fact that at low frequencies there is more inspiral part of the waveform in the frequency band, and therefore, the inability of the quasicircular model to resemble the eccentric inspiral becomes notorious. One can also appreciate in Fig. 6 that generally the higher the initial eccentricity the higher the mismatch for the whole mass range.

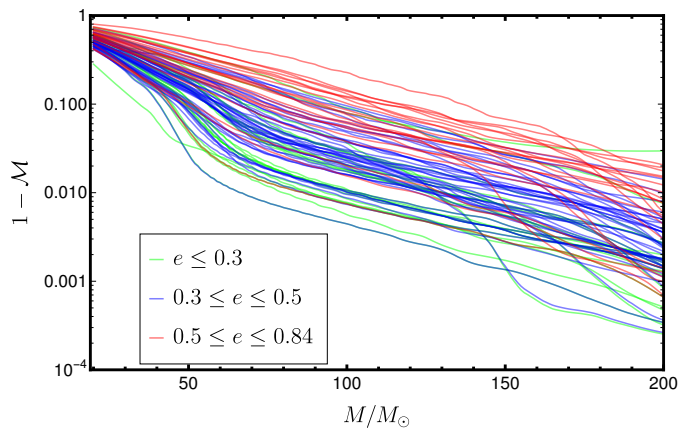


Figure 6: Mismatches for the $(l, m) = (2, 2)$ mode between the eccentric hybrid waveforms corresponding to the cases presented in Table IV of Appendix A and the quasicircular PhenomX waveform model as a function of the total mass of the system. The green, blue, black and red lines correspond to eccentric PN-NR hybrid waveforms with initial eccentricities $e \leq 0.3$, $0.3 \leq e \leq 0.5$ and $0.5 \leq e \leq 0.84$, respectively.

B. Eccentric Injections into detector noise

In this section we show some applications of the eccentric waveform data set to parameter estimation. We inject eccentric hybrids into Gaussian noise realization recolored to match the spectral density of the Advanced LIGO and Virgo detectors at design sensitivity. All simulations with the same injected signal are performed with the same noise realization. We do not address the challenge of detecting eccentric signals and instead assume that the signal has been detected by standard CBC search pipelines [69]. We perform parameter estimation using the python-based BILBY code [70]. Of the numerous stochastic samplers implemented in BILBY, we employ the nested sampler CPNEST [71] and use waveform approximants implemented in LALSUITE [64] as the model templates. The eccentric hybrids make use of the Numerical Relativity injection infrastructure [72, 73].

At the time of writing, the state of the art non-spinning eccentric IMR models [31–34] were not yet implemented in LALSUITE. The only eccentric waveform models in LALSUITE are inspiral non-spinning frequency domain approximants [28, 74, 75]. We decide not to use such inspiral waveform models to avoid biases induced by the sharp cutoff at the end of the waveform [76]. For a study of the eccentricity measurement using such inspiral approximants see [77]. We restrict to IMR quasicircular approximants and perform parameter estimation analysis on the injected eccentric signals sampling on the 15 parameters of a quasicircular black-hole binary.

We inject three NR equal mass non-spinning simulations described in Table I into a network of gravitational wave detectors composed of the LIGO-Hanford, LIGO-Livingston [78] and Virgo interferometers [79], each operating at design sensitivity. We set a reference frequency of $f_{\text{ref}} = 20$ Hz, where the waveforms start. Some injected parameters are

ID	Simulation	q	$\chi_{1,z}$	$\chi_{2,z}$	D/M	$e_\omega \pm \delta e_\omega$
61	SXS:BBH:1355	1.	0.	0.	12.97	0.090 ± 0.003
62	SXS:BBH:1359	1.	0.	0.	15.73	0.146 ± 0.003
63	SXS:BBH:1361	1.	0.	0.	16.69	0.209 ± 0.003

Table I: Summary of the eccentric NR simulations injected. The first column denotes the identifier of the simulation, the second column indicates the name of the simulation as presented in [32]. Next columns show the mass ratio, z-component of the dimensionless spin vectors, the initial orbital separation and the initial orbital eccentricity as measured using the procedure detailed in Sec. II D.

displayed in Table II, while the declination is $\delta = -1.21$ rad, the right ascension $\alpha = 1.37$ rad and the coalescence phase $\phi = 0$ rad. From these simulations, the $\{(l, m) = \{(2, \pm 2), (3, \pm 2), (4, \pm 4), (5, \pm 4), (6, \pm 6)\}$ modes are used, we do not inject odd m modes because they are zero by symmetry. For the injected signal we choose the luminosity distance similar to the first detection of a gravitational wave signal, GW150914 [7], which produces a high network signal-to-noise ratio (SNR) as shown in Tables II, III.

We employ a uniform-in-volume prior on the luminosity distance, $p(D_L|H) \propto D_L^2$, between 50 and 1500 Mpc. The inclination and polarization angles have both uniform priors between $(0, \pi)$. We use the standard priors for the extrinsic variables, as in Table I of [70]. Instead of sampling in the component masses we sample in the mass ratio, q, and the chirp mass, \mathcal{M}_c , with a range $(0.05, 1)$ and $(15, 60)M_\odot$, respectively. The spin priors are set differently according to the approximant. If the approximant is non-precessing, we set the option of `aligned_spin=True` in the `BBHPriorDict` function in Bilby which does not sample neither in the tilt angles, (θ_1, θ_2) , the angle between the spin vectors, ϕ_{12} , nor the angle between \mathbf{J} and \mathbf{L} , ϕ_{JL} , instead it samples on the spin z-components between -0.8 and +0.8. While if the approximant is precessing the priors for $a_1, a_2, \theta_1, \theta_2, \phi_{JL}$ and ϕ_{12} are the same as in Table I of [70]. We also define a uniform prior for the coalescence time with minimum and maximum at one second of the injection time. For the CPNEST sampler we take the number of live points $N_{\text{live}} = 16824$ and `max-mcmc` = 5000. This is a computationally expensive setup aiming to ensure an accurate sampling of the likelihood given the complexity of the signal.

We take three quasicircular models as approximants, IMRPhenomD [12, 67], non-precessing model with only the $(2, \pm 2)$ modes, IMRPhenomHM [15], non-precessing model including higher order modes, and IMRPhenomPv2 [13], effective precessing model. We plot the posterior probability distribution for the chirp mass, mass ratio, effective spin parameter and luminosity distance for the three approximants in Fig. 7 with 90% credible intervals specified by the dashed lines and the injected values by the magenta thick vertical lines. The fainter the colour of the posterior distributions the lower the initial eccentricity. The same information is summarized in Fig. 10, where the median and the error bars corresponding to the 90% credible intervals of the posterior dis-

tribution are shown as a function of the initial eccentricity. Note that the bars corresponding to the same initial eccentricity but different approximants have been separated by a small amount to ease the visualization of the results. For the lowest initial eccentricity, $e_0 = 0.09$ the results for the four quantities are pretty different. The chirp mass and the effective spin parameter produce similar distributions for the three approximants, while for the mass ratio and the luminosity distance PhenomHM distributions are closer to the injected values than PhenomD and PhenomPv2. Furthermore, for $e_0 = 0.14$ and $e_0 = 0.2$ we observe increasing error bars in the parameters and a poorer agreement with the injected values, except for the mass ratio where the lowest initial eccentricity signal produces larger errors than the ones with higher initial eccentricity. This can also be checked in Table II, where the recovered parameters, median values and 90% credible intervals, are compared to the injected values. Regarding the effective spin parameter and the chirp mass, the increase of initial eccentricity in the injected signal shifts the posteriors for the three quasicircular models, while for the mass ratio the increase of initial eccentricity reduces the bias on the measurement of the mass ratio, probably as a consequence of the shift in the chirp mass distribution. One observes also that PhenomHM recovers better the injected parameters than PhenomD and PhenomPv2. For the luminosity distance the probability densities

tend to flatten and be closer to the prior distributions for high initial eccentricities, one notes again that PhenomHM has less parameter bias than PhenomD and PhenomPv2. Injected values of the sky position like the right ascension $\alpha = 1.375$ rad and $\delta = -1.21$ rad are well recovered for all the runs: $\alpha = 1.37^{+0.01}_{-0.01}$ rad and $\delta = -1.21^{+0.01}_{-0.01}$ rad. Furthermore, we have computed the recovered matched-filter SNR for the detector network, ρ_{Match} , for each simulation. This quantity, ρ_{Match} , is computed calculating the matched filter between the detector data with the eccentric signal injected and the waveform of the approximant waveform model with the parameters corresponding to the lowest loglikelihood value of the posterior distribution. The results of such a calculation are shown in Table I. Additionally, we display the values of the log Bayes factor for each simulation. One can observe that both the recovered matched-filter SNR and the log Bayes factor decrease the higher the initial eccentricity of the injected signal. The reweighted SNR produces similar values between models for simulation with the same initial eccentricity. However, the log Bayes factor tends to be slightly higher for aligned-spin waveform models, PhenomD and PhenomHM, for the lowest initial eccentric injected signal, while for higher initial eccentricities the precessing model IMRPhenomPv2 shows slightly greater log Bayes factors than the aligned-spin ones.

We repeat the same procedure injecting a hybrid waveform, including only the $(l, m) = (2, \pm 2)$ mode, of an eccentric spinning waveform with ID 8 of Table IV. This is an equal mass with the z-component of the dimensionless spin vectors $\chi_{1z} = \chi_{2z} = -0.25$ and initial eccentricity $e_0 = 0.420 \pm 0.006$. The posterior distribution for the chirp mass, mass ratio, luminosity distance and χ_{eff} are shown in Fig. 8 for the IMRPhenomD, IMRPhenomHM and IMRPhenomPv2 as waveform models. In this case the parameter biases are much higher than in the previous injection study mainly due to the fact that the injected signal has a much higher initial eccentricity. The values of the recovered parameters as well as the injected values are shown in Table III. The injected values of the sky position like the right ascension $\alpha = 1.375$ rad and $\delta = -1.21$ rad are again well recovered parameters for the three runs $\alpha = 1.37^{+0.01}_{-0.01}$ rad and $\delta = -1.21^{+0.01}_{-0.01}$ rad. The bias in the chirp mass is $\sim 4M_{\odot}$ for the three models. Here one can observe the correlation between chirp mass and mass ratio, the shift in chirp mass posteriors with respect to the injected value translates into a better determined mass ratio distribution, which is clearly the case for PhenomHM which performs unexpectedly well recovering the mass ratio parameter, while PhenomD and PhenomPv2 show much wider distributions and much larger credible intervals. The posteriors of the luminosity distance show also large error bars for the three

models, where again PhenomHM reduces the bias with respect to PhenomD and PhenomPv2. The recovered effective spin parameter is completely off with respect to the injected value for the three approximants. The recovered χ_{eff} is positive while the injected one is negative, the bias in the effective spin parameter is approximately -0.3 for the three models, indicating the inability of the quasicircular models to estimate the spin parameter of highly eccentric spinning binaries with quasicircular models. Regarding the recovered matched-filter SNR and the log Bayes factor displayed in Table III one can observe that while the SNR provides comparable values among models, the values of the log Bayes factor indicate that PhenomPv2 fits scarcely better the data than PhenomHM and PhenomD.

This section shows examples of the kind of study that one is able to perform with the current eccentric waveform data set. We have shown the limitations of the current IMR quasicircular to estimate the parameters of moderately eccentric waveforms including a moderately spinning case. For the cases studied in this section we have found that although the use of quasicircular models to estimate parameters of eccentric signals leads to inevitable biases, aligned spin quasicircular models with higher order modes leverage the impact of this biases for the mass ratio and the luminosity distance when compared to aligned spin models with only the $(2, \pm 2)$ modes

e_0	Model	m_1/M_\odot	m_2/M_\odot	M_c/M_\odot	q	D_L/Mpc	χ_{eff}	ψ (rad)	ι (rad)	ρ_{Match}	$\log \mathcal{B}$
0.09	PhenomD	$35.06^{+2.55}_{-1.92}$	$31.29^{+1.10}_{-1.33}$	$28.40^{+0.17}_{-0.17}$	$0.87^{+0.10}_{-0.12}$	384^{+49}_{-82}	$0.00^{+0.02}_{-0.02}$	$1.60^{+1.28}_{-1.34}$	$0.54^{+0.32}_{-0.32}$	89.40	3463.79
	PhenomHM	$34.05^{+2.14}_{-1.16}$	$31.79^{+0.69}_{-1.17}$	$28.38^{+0.16}_{-0.16}$	$0.92^{+0.07}_{-0.11}$	429^{+16}_{-33}	$-0.01^{+0.02}_{-0.02}$	$2.01^{+0.97}_{-1.82}$	$0.28^{+0.21}_{-0.17}$	89.28	3463.78
	PhenomPv2	$35.26^{+2.97}_{-2.06}$	$31.28^{+1.18}_{-1.53}$	$28.44^{+0.21}_{-0.18}$	$0.86^{+0.11}_{-0.13}$	412^{+24}_{-66}	$0.00^{+0.02}_{-0.02}$	$1.65^{+1.22}_{-1.32}$	$0.39^{+0.32}_{-0.22}$	89.19	3459.54
0.14	PhenomD	$34.03^{+1.34}_{-0.72}$	$32.63^{+0.44}_{-0.73}$	$28.86^{+0.15}_{-0.15}$	$0.95^{+0.04}_{-0.07}$	407^{+53}_{-84}	$0.02^{+0.02}_{-0.02}$	$1.58^{+1.21}_{-1.23}$	$0.54^{+0.32}_{-0.32}$	84.87	3288.25
	PhenomHM	$33.76^{+0.96}_{-0.54}$	$32.73^{+0.35}_{-0.56}$	$28.82^{+0.16}_{-0.14}$	$0.96^{+0.03}_{-0.05}$	408^{+46}_{-52}	$0.02^{+0.02}_{-0.02}$	$1.91^{+0.46}_{-0.58}$	$0.54^{+0.19}_{-0.25}$	84.74	3283.61
	PhenomPv2	$34.22^{+1.48}_{-0.89}$	$32.54^{+0.54}_{-0.82}$	$28.87^{+0.19}_{-0.21}$	$0.94^{+0.05}_{-0.08}$	389^{+33}_{-60}	$0.01^{+0.02}_{-0.03}$	$1.70^{+1.09}_{-1.07}$	$0.64^{+0.25}_{-0.18}$	85.08	3302.37
0.2	PhenomD	$35.65^{+1.52}_{-0.85}$	$34.01^{+0.51}_{-0.82}$	$30.13^{+0.16}_{-0.16}$	$0.94^{+0.05}_{-0.07}$	420^{+72}_{-109}	$0.07^{+0.02}_{-0.02}$	$1.57^{+1.36}_{-1.18}$	$0.61^{+0.41}_{-0.37}$	81.88	3102.70
	PhenomHM	$35.47^{+1.36}_{-0.78}$	$33.97^{+0.46}_{-0.72}$	$30.06^{+0.16}_{-0.15}$	$0.95^{+0.04}_{-0.07}$	438^{+43}_{-47}	$0.06^{+0.02}_{-0.02}$	$0.42^{+0.90}_{-0.29}$	$0.54^{+0.16}_{-0.20}$	81.97	3101.79
	PhenomPv2	$37.13^{+2.11}_{-1.76}$	$33.20^{+1.00}_{-1.12}$	$30.12^{+0.21}_{-0.22}$	$0.87^{+0.09}_{-0.09}$	414^{+41}_{-69}	$0.06^{+0.02}_{-0.02}$	$1.62^{+0.98}_{-1.29}$	$0.66^{+0.25}_{-0.18}$	82.05	3112.97
	Injected	32.5	32.5	28.29	1.	430	0.	0.33	0.3		

Table II: Black hole binary recovered parameters for the three NR simulations from Table I. The last row corresponds to the injected parameters. The first column describes the initial eccentricity of the injected signal, then we specify the approximant, the component masses, the chirp mass, mass ratio, luminosity distance, effective spin parameter, polarization angle, inclination, the recovered matched-filter SNR for the detector network and the log of the Bayes factor.

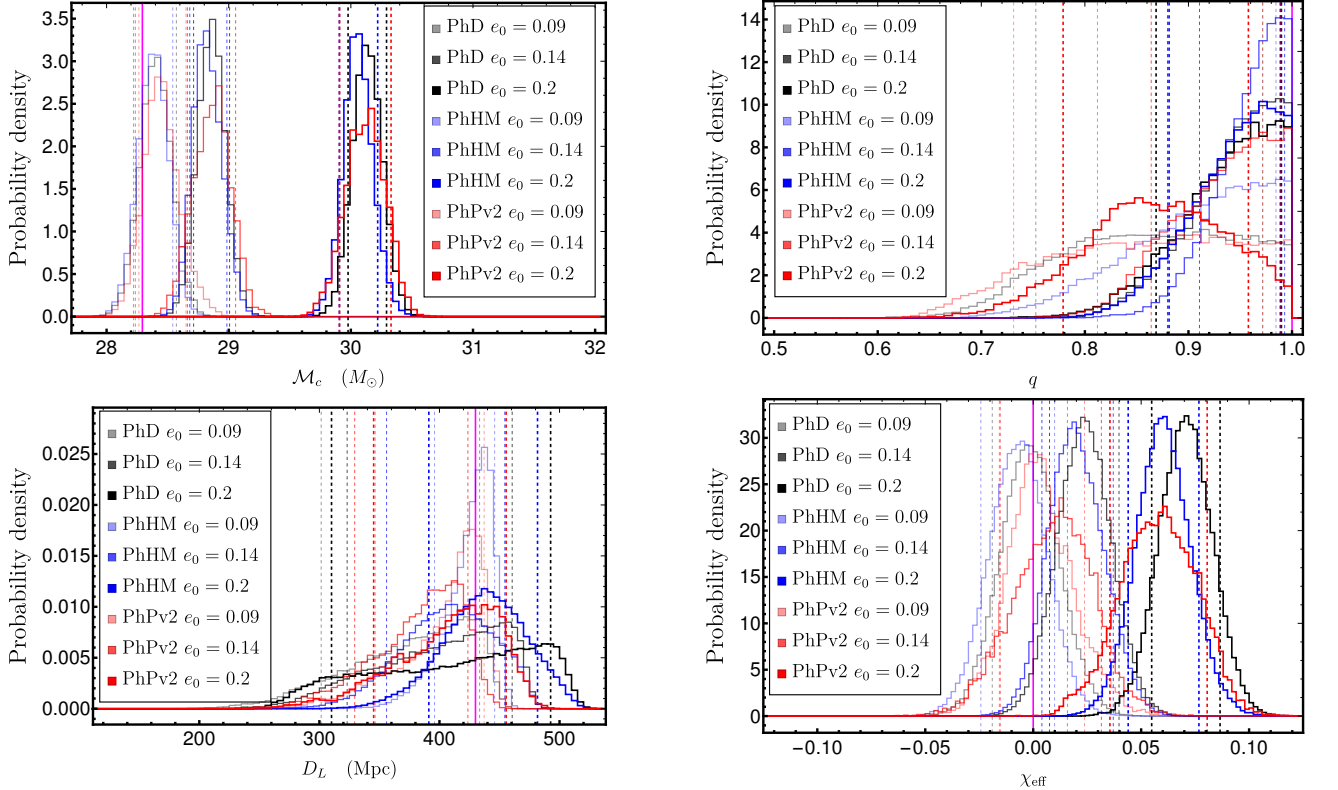


Figure 7: Posterior probability distributions for the injected NR simulations of Table I. The vertical dashed lines correspond to 90% credible regions. The magenta thick vertical line represents the injected value. The black, blue and red curves represent distributions sampled using the IMRPhenomD, IMRPhenomHM and IMRPhenomPv2 approximants, respectively. With increasingly higher opacity are represented injections with initial eccentricities, $e_0 = 0.09, 0.14, 0.2$.

or precessing models. Due to the computational cost of the PE runs and the amount of eccentric waveforms available we leave for future work a detailed study of the whole data set using not only quasicircular models, but also eccentric waveform approximants.

V. SUMMARY AND CONCLUSIONS

In this paper we have presented the first parameter study of numerical relativity simulations of eccentric spinning black-

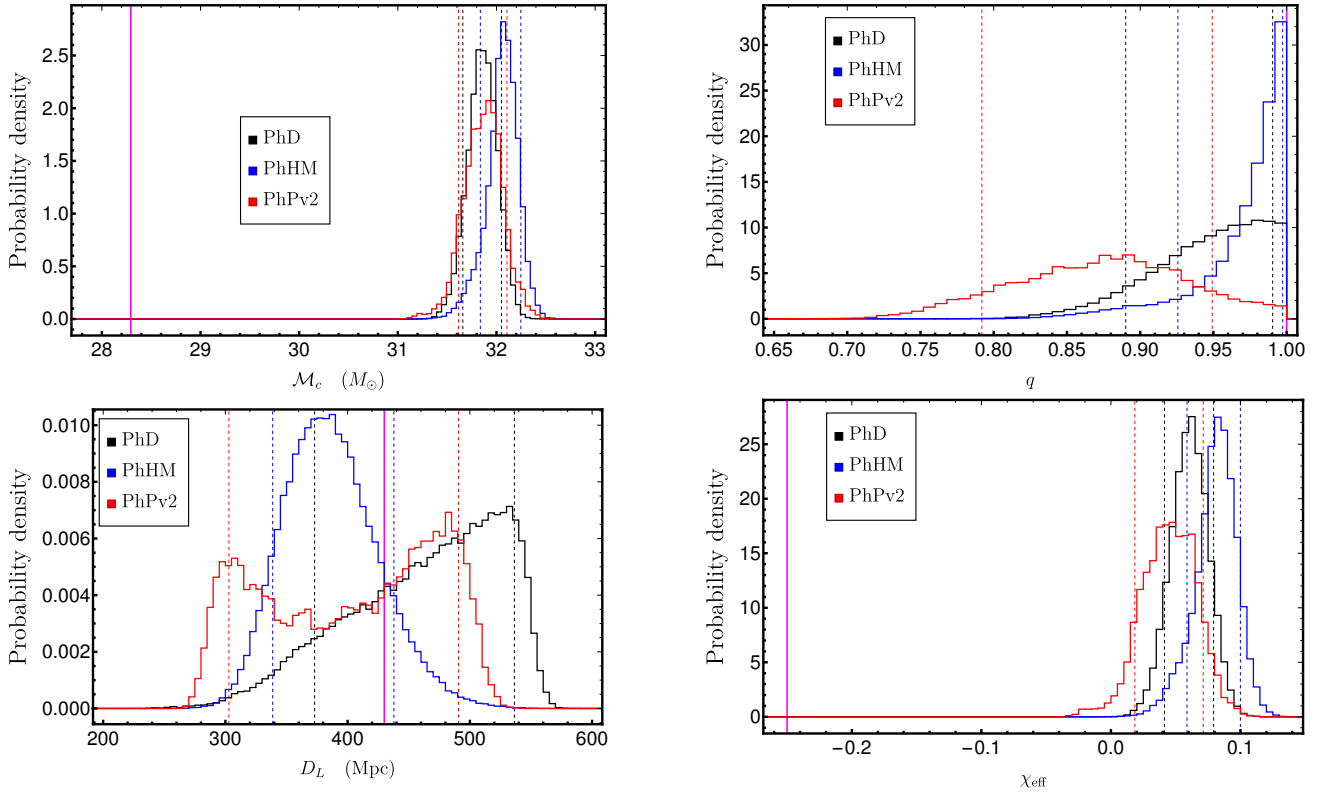


Figure 8: Posterior probability distributions for the injected spinning eccentric hybrid waveform, with initial eccentricity $e_0 = 0.420 \pm 0.006$. The vertical dashed lines correspond to 90% credible regions. The magenta thick vertical line represents the injected value. The black, blue and red curves represent distributions sampled using the IMRPhenomD, IMRPhenomHM and IMRPhenomPv2 approximants, respectively.

e_0	Model	m_1/M_\odot	m_2/M_\odot	M_c/M_\odot	q	D_L/Mpc	χ_{eff}	ψ (rad)	ι (rad)	ρ_{Match}	$\log \mathcal{B}$
0.42	PhenomD	$37.52^{+1.30}_{-0.76}$	$36.04^{+0.49}_{-0.73}$	$31.86^{+0.19}_{-0.2}$	$0.95^{+0.04}_{-0.06}$	474^{+62}_{-101}	$0.06^{+0.02}_{-0.02}$	$2.60^{+0.31}_{-0.33}$	$1.54^{+1.22}_{-1.19}$	82.68	2895.91
	PhenomHM	$37.23^{+0.95}_{-0.37}$	$36.62^{+0.30}_{-0.81}$	$32.07^{+0.18}_{-0.23}$	$0.98^{+0.02}_{-0.06}$	384^{+54}_{-45}	$0.08^{+0.02}_{-0.02}$	$2.28^{+0.18}_{-0.16}$	$1.04^{+1.12}_{-0.26}$	82.54	2894.17
	PhenomPv2	$39.15^{+2.08}_{-1.62}$	$35.20^{+0.84}_{-1.06}$	$31.87^{+0.23}_{-0.26}$	$0.88^{+0.07}_{-0.08}$	413^{+77}_{-110}	$0.05^{+0.03}_{-0.03}$	$2.33^{+0.33}_{-0.44}$	$1.46^{+1.36}_{-0.45}$	82.62	2910.28
	Injected	32.5	32.5	28.29	1.	430	-0.25	0.33	0.3		

Table III: Black hole binary recovered parameters for the spinning hybrid waveform from Fig. 8. The last row corresponds to the injected parameters. The first column describes the initial eccentricity of the injected signal, then we specify the approximant, the component masses, the chirp mass, mass ratio, luminosity distance, effective spin parameter, polarization angle, inclination, the recovered matched-filter SNR for the detector network and the log of the Bayes factor.

hole binaries. We have presented a simple procedure to set up the initial parameters of eccentric simulations. The higher the initial eccentricity of the simulation the longer the initial separation has to be in order to avoid the immediate plunge of the binary due to the strong interactions at the periastron. This increases the computational cost of the simulations of Table IV with $e_0 \sim 0.4$ which is roughly double the one with $e_0 \sim 0.2$ as can be observed in their merger times. Additionally, longer initial separations produce long enough waveforms which allow to avoid the breakdown of the post-Newtonian approximation and ease the posterior construction of PN-NR hybrid waveforms. As part of the post-processing step, we have computed the final mass and final spin of the 60 new simulations

presented in Table IV. We have compared the final mass and final spin of those simulations with quasicircular NR fits [42] and found that relative differences are as high as 1%, which is completely consistent with the inaccuracies of the fitting formulae and gauge transient in the apparent horizon quantities. Therefore, we have extended previous work [37] on the circularization of eccentric non-spinning Numerical Relativity simulations to the eccentric spinning case. Note that the eccentricities of the simulations presented in this communication have more moderate values than the ones presented in [37], although ours are much longer and include spins.

Crucial part of these work has been to extend the low eccentric procedure to measure the eccentricity in NR [39] to the

arbitrary high eccentric limit. We have shown that eccentricity estimator used in [39] cannot be used for high eccentricities because it does not reduce to the Newtonian definition of the eccentricity. Additionally, its reliance on a non-eccentric fit makes it numerically inaccurate and it can produce eccentricity values higher than 1. As a consequence, we have decided to use another eccentricity estimator [48] constructed also upon the orbital frequency and which does not rely on any non-eccentric fit. This eccentricity estimator reduces to the Newtonian definition of eccentricity for arbitrarily high eccentricities. We have shown that with this eccentricity estimator we are able to robustly measure the eccentricity for the whole evolution, which will be a key result to generate a future eccentric waveform model.

We have then taken the NR waveforms and hybridized the (2, 2) mode with PN waveforms. The production of the eccentric PN waveforms has required to solve the point particle 3.5PN equations of motion in ADMTT coordinates [39] enhanced with the eccentric contribution to the energy flux from [51]. The absence of complete generic PN expressions for the waveform modes has caused the inaccuracy of the PN waveforms to dominate the error in the hybridization procedure. The use of the instantaneous terms at 3PN order [53] produces inaccurate waveforms due to the lack of the low order tail terms, while the full 3PN expressions in [54] are restricted to the QK parametrization and rely on a certain decomposition of the dynamical variables which complicates their combination with the generic numerical solution of the equations of motion (3.1). Therefore, we have restricted to the use of the quadrupole formula with a correction procedure for the initial orbital separation. We have developed a procedure which corrects the initial orbital separation of the PN evolution code for a certain δr , such that it minimizes the difference in amplitude between the PN and NR (2, 2) waveforms modes. We have shown that with that procedure we are left with relative errors in the amplitude and phase below 1% in the hybridization region. These errors in amplitude and phase are high compared to the quasicircular ones [80], where the PN knowledge is wider. Therefore, we expect that in the future an improvement in the knowledge of the post-Newtonian waveforms will allow us to construct more accurate hybrid waveforms, not only for the (2, 2) mode, but also for the higher order modes.

We have also compared the hybrid waveforms with quasicircular IMR waveform models. This has been done first computing the mismatch of the eccentric hybrid data set against the quasicircular non-precessing PhenomX model [18, 19]. We find that the mismatches become much higher than 3% for binaries with a total mass lower than $100M_{\odot}$, while for total masses higher than $150M_{\odot}$, the mismatch lowers below 3% due to the fact that most of the eccentric waveform in the frequency band of the detector is in the merger-ringdown parts, which as shown in Sec. II C, due to circularization agrees really well with the quasicircular model.

Additionally, we have made a set of injection into gaussian detector noise colored to match the LIGO and Virgo design detector sensitivities. We have studied the parameter biases on recovered parameters when using quasicircular models as approximants. We have used three different quasicircular mod-

els to recover the parameters and shown that, although the use of quasicircular models leads to inevitable biases in parameters like the effective spin parameter or the chirp mass, where the biases are similar among the three models, others like the mass ratio and the luminosity distance present lower biases when using quasicircular aligned spin models including higher order modes. Another important feature is the correlation between chirp mass and mass ratio, the better the measurement of the chirp mass the worse the determination of the mass ratio and viceversa, and this can be clearly observed in Figs. 7 and 8 where for initial eccentricities 0.09 the chirp mass is well measured for the three models, but the mass ratio distributions are not and as the initial eccentricity increases so does the shift in the chirp mass distribution and generally the better the mass ratio is determined. In the case of the spinning eccentric hybrid the high initial eccentricity produces clear biases in all the quantities and unexpectedly PhenomHM recovers well the injected value of the mass ratio and performs the best for the luminosity distance. The study of this phenomenology for the different cases that we have available is ongoing and we leave for a future communication the extension of these results to the whole parameter space.

The work presented in this communication is a natural extension of [39]. We have set up the current infrastructure of our group for quasicircular waveform modelling to the eccentric case. As shown in this paper, we have developed new methods to produce a set of spinning eccentric hybrid waveforms which can actually be used for data analysis purposes. The next natural step is to use this hybrid data set to produce a calibrated eccentric IMR waveform, which can be used for detection and parameter estimation of eccentric black-hole binaries.

VI. ACKNOWLEDGEMENTS

We thank Frank Ohme for useful comments about manuscript and Maria Haney for valuable discussions. This work was supported by European Union FEDER funds, the Ministry of Science, Innovation and Universities and the Spanish Agencia Estatal de Investigación grants FPA2016-76821-P, FPA2017-90687-REDC, FPA2017-90566-REDC. FIS2016-81770-REDC, FPA2015-68783-REDC, the Spanish Ministry of Education, Culture and Sport grants FPU15/03344, FPU15/01319, Vicepresidència i Conselleria d'Innovació, Recerca i Turisme, Conselleria d'Educació, i Universitats del Govern de les Illes Balears i Fons Social Europeu, Generalitat Valenciana (PROMETEO/2019/071), EU COST Actions CA18108, CA17137, CA16214, and CA16104, H2020-MSCA-IF-2016. Marie Skłodowska-Curie Individual Fellowships Proposal number: 751492. The authors thankfully acknowledge the computer resources at MareNostrum and the technical support provided by Barcelona Supercomputing Center (BSC) through Grants No. AECT-2019-2-0010, AECT-2019-1-0022, AECT-2018-3-0017, AECT-2018-2-0022, AECT-2018-1-0009, AECT-2017-3-0013, AECT-2017-2-0017, AECT-2017-1-0017, AECT-2016-3-0014, AECT2016-2-0009, from

the Red Española de Supercomputación (RES) and PRACE (Grant No. 2015133131). BAM and ET simulations were carried out on the BSC MareNostrum computer under PRACE and RES (Red Española de Supercomputación) allocations and on the FONER computer at the University of the Balearic Islands.

Appendix A: Numerical Relativity Simulations

The numerical set up for the BAM and the EinsteinToolkit codes is the same described in Appendix C of [39]. We present in Table IV the NR simulations we have produced for this publication.

Appendix B: Eccentricity estimators in highly eccentric systems

In this section we briefly show the form of the eccentricity estimators of Eqs. (2.7) and (2.8) in the Newtonian limit. We start analyzing the eccentricity estimator

$$e_\omega(t) = \frac{\omega(t) - \omega(e=0)}{2\omega(e=0)}. \quad (\text{B1})$$

In the Keplerian parametrization the orbital frequency can be written as:

$$\omega(t) = \frac{n_t \sqrt{1-e^2}}{(1-e \cos u)^2}, \quad (\text{B2})$$

where $n_t = 2\pi/T_{\text{orb}}$ is the mean motion, T_{orb} is the orbital period, e is the eccentricity and u is the eccentric anomaly. In the low eccentric limit, Eq. (B1) reduces to

$$\omega(t) \approx n_t [1 + 2e \cos u] + \mathcal{O}(e^2). \quad (\text{B3})$$

Replacing Eq. (B3) in Eq. (B1) one obtains $e_\omega = e$. However, if one substitutes Eq. (B2) in Eq. (B1) one gets

$$e_\omega(t) = \frac{1}{2} \left(\frac{\sqrt{1-e^2}}{[e \cos(u) - 1]^2} - 1 \right), \quad (\text{B4})$$

which does not reduce to the Newtonian definition of eccentricity. Moreover, one can show that the estimator of Eq. (B4) is not normalized for a certain combination of values of u and e . For example, if u vanishes, then

$$e_\omega \geq 1 \quad \text{for} \quad e \geq 0.455212. \quad (\text{B5})$$

This shows that the eccentricity estimator given by Eq. (B1) has to be taken with caution in the high eccentric limit because it can go above 1. On the other hand, the eccentricity estimator

$$e_{\Omega_{a,p}}(t) = \frac{\omega_p^{1/2} - \omega_a^{1/2}}{\omega_p^{1/2} + \omega_a^{1/2}}, \quad (\text{B6})$$

where ω_a, ω_p are the orbital frequency at the apastron and periastron, respectively. This eccentricity estimator has the property that even for high eccentricities it reduces to the Newtonian definition of eccentricity, i.e., $e_{\Omega_{a,p}} = e$.

Appendix C: Error bars of the posterior distributions

In this section we show the median values error bars corresponding to the 90% credible intervals in the posterior distribution for the mass ratio, chirp mass, luminosity distance and effective spin parameter for the injected signals in Table I. The errors bars and median values for different initial eccentricities are shown in Fig. 7.

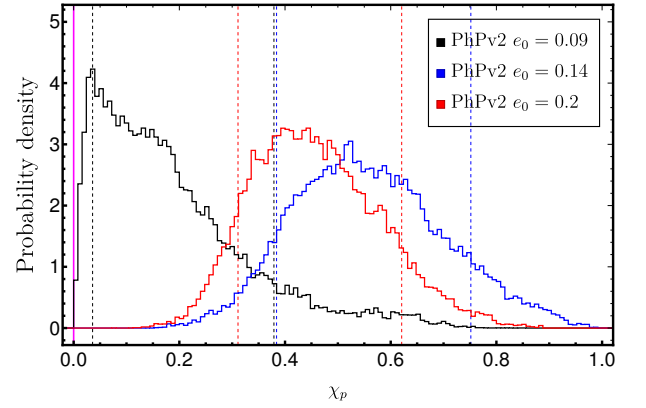


Figure 9: Posterior probability distributions of χ_p for the injected NR simulations of Table I. The vertical dashed lines correspond to 90% credible regions. The magenta thick vertical line represents the injected value. The black, blue and red curves represent injections with initial eccentricities, $e_0 = 0.09, 0.14, 0.2$. All cases are sampled using as approximant IMRPhenomPv2.

For completion we also show in Fig. 9 the posterior distribution of the χ_p parameter for the NR simulations of Fig. 1 run with IMRPhenomPv2. This parameter, defined in [81], accounts for the spin components orthogonal to the direction of the orbital angular momentum vector of the system. Therefore, for non-precessing configurations $\chi_p = 0$ and for precessing configurations it ranges between 0 and 1. In Fig. 9 one can observe an increase in χ_p with increasing initial eccentricity of the injected signal. This result means that the precessing waveform IMRPhenomPv2 is trying to compensate the inability to reproduce the eccentric signal incrementing the value of the χ_p parameter, i.e., increasing the precession.

ID	Simulation	Code	q	$\chi_{1,z}$	$\chi_{2,z}$	χ_{eff}	D/M	$e_\omega \pm \delta e_\omega$	T_{merger}/M	N_{orbits}	M_f	χ_f
1	q1...0...D12.23.lam96	BAM	1.	0.	0.	0.	12.23	0.114 ± 0.002	1256.42	4.5	0.9527	0.6871
2	q1...0...D15.lam915	BAM	1.	0.	0.	0.	15.0	0.210 ± 0.002	1682.01	5.2	0.9533	0.6895
3	q1...0...D15.lam96	BAM	1.	0.	0.	0.	15.0	0.095 ± 0.002	2961.01	8.3	0.9525	0.6869
4	q1...0...D17.lam915	BAM	1.	0.	0.	0.	17.0	0.195 ± 0.003	2917.42	8.2	0.9535	0.6889
5	q1...0...D20	BAM	1.	0.	0.	0.	30.0	0.301 ± 0.001	497.48	1.5	0.9548	0.6950
6	Eccq1...0...0.25...et0.1.D14	ET	1.	0.	0.25	0.125	14.0	0.100 ± 0.002	2319.85	6.4	0.9480	0.7249
7	Eccq1...0...0.25...et0.2.D16	ET	1.	0.	0.25	0.125	16.0	0.217 ± 0.003	2449.84	5.8	0.9474	0.7243
8	Eccq1...-0.25...-0.25...et0.1.D12	ET	1.	-0.25	-0.25	-0.25	12.0	0.148 ± 0.002	939.87	2.8	0.9579	0.6080
9	Eccq1...0.25...0.25...et0.1.D12	ET	1.	0.25	0.25	0.25	12.0	0.131 ± 0.002	1347.59	4.8	0.9440	0.7605
10	Eccq1...-0.25...-0.25...et0.1.D14	ET	1.	-0.25	-0.25	-0.25	14.0	0.134 ± 0.002	1897.26	5.3	0.9573	0.6091
11	Eccq1...0.25...0.25...et0.1.D14	ET	1.	0.25	0.25	0.25	14.0	0.112 ± 0.003	2464.75	7.6	0.9440	0.7607
12	Eccq1...-0.25...-0.25...et0.2.D14	ET	1.	-0.25	-0.25	-0.25	14.0	0.249 ± 0.002	1067.25	3.8	0.9578	0.6109
13	Eccq1...0.25...0.25...et0.2.D14	ET	1.	0.25	0.25	0.25	14.0	0.194 ± 0.002	1499.92	5.0	0.9432	0.7620
14	Eccq1...0.25...0.25...et0.2.D16	ET	1.	0.25	0.25	0.25	16.0	0.199 ± 0.003	2599.90	8.9	0.9437	0.7624
15	Eccq1...-0.25...-0.25...et0.5.D26	ET	1.	-0.25	-0.25	-0.25	26.0	0.38 ± 0.004	3287.31	7.7	0.9566	0.6080
16	Eccq1...0.25...0.25...et0.5.D26	ET	1.	0.25	0.25	0.25	26.0	0.418 ± 0.004	4613.02	11.3	0.9428	0.7604
17	Eccq1...0.25...0...et0.1.D14	ET	1.	0.25	0.	0.125	14.0	0.128 ± 0.003	2302.69	7.2	0.9480	0.7249
18	Eccq1...0.25...0...et0.2.D16	ET	1.	0.25	0.	0.125	16.0	0.161 ± 0.002	2411.27	7.4	0.9474	0.7242
19	Eccq1...-0.5...-0.5...et0.1.D13	ET	1.	-0.5	-0.5	-0.5	13.0	0.143 ± 0.002	1131.58	3.2	0.9623	0.5286
20	Eccq1...0.5...0.5...et0.1.D13	ET	1.	0.5	0.5	0.5	13.0	0.116 ± 0.002	2071.02	7.3	0.9323	0.8309
21	Eccq1...-0.5...-0.5...et0.2.D15	ET	1.	-0.5	-0.5	-0.5	15.0	0.104 ± 0.001	1170.51	3.3	0.9624	0.5298
22	Eccq1...0.5...0.5...et0.2.D15	ET	1.	0.5	0.5	0.5	15.0	0.194 ± 0.002	2290.43	7.7	0.9329	0.8323
23	Eccq1...-0.5...-0.5...et0.5.D26	ET	1.	0.5	0.5	0.5	26.0	0.505 ± 0.005	2675.44	6.1	0.9622	0.5230
24	Eccq1...0.5...0.5...et0.5.D26	ET	1.	0.5	0.5	0.5	26.0	0.400 ± 0.004	5307.53	13.4	0.9322	0.8294
25	Eccq1...-0.75...-0.75...et0.1.D13	ET	1.	-0.75	-0.75	-0.75	13.0	0.144 ± 0.002	907.44	2.5	0.9654	0.4458
26	Eccq1...0.75...0.75...et0.1.D13	ET	1.	0.75	0.75	0.75	13.0	0.089 ± 0.002	2307.95	8.3	0.9156	0.8934
27	Eccq1...-0.75...-0.75...et0.2.D15	ET	1.	-0.75	-0.75	-0.75	15.0	0.249 ± 0.002	902.561	2.6	0.9657	0.4475
28	Eccq1...0.75...0.75...et0.2.D15	ET	1.	0.75	0.75	0.75	15.0	0.181 ± 0.002	2629.47	9.5	0.9149	0.8904
29	Eccq1...-0.75...-0.75...et0.5.D26	ET	1.	-0.75	-0.75	-0.75	26.0	0.339 ± 0.003	2079.87	4.1	0.9655	0.4506
30	Eccq1...0.75...0.75...et0.5.D26	ET	1.	0.75	0.75	0.75	26.0	0.373 ± 0.004	5907.6	15.1	0.9158	0.8843
31	Eccq1.5...0...0...et0.1.D13	ET	1.5	0.	0.	0.	13.0	0.108 ± 0.002	1606.33	5.2	0.9552	0.6651
32	Eccq1.5...0...0...et0.2.D13.5	ET	1.5	0.	0.	0.	13.5	0.126 ± 0.001	1142.56	3.8	0.9553	0.6619
33	Eccq1.5...0...0...et0.2.D15	ET	1.5	0.	0.	0.	15.0	0.245 ± 0.002	1809.34	5.4	0.9548	0.6636
34	Eccq2...0...0...et0.1.D13	ET	2.	0.	0.	0.	13.0	0.106 ± 0.002	1738.71	5.3	0.9610	0.6232
35	Eccq2...0...0...et0.2.D16	ET	2.	0.	0.	0.	16.0	0.167 ± 0.002	2499.02	7.5	0.9610	0.6249
36	Eccq2...0...0...et0.5.D26	ET	2.	0.	0.	0.	26.0	0.422 ± 0.004	4380.33	10.4	0.9609	0.6262
37	Eccq2...-0.25...-0.25...et0.1.D12	ET	2.	-0.25	-0.25	-0.25	12.0	0.138 ± 0.002	1026.39	3.2	0.9664	0.5283
38	Eccq2...0.25...0.25...et0.1.D12	ET	2.	0.25	0.25	0.25	12.0	0.103 ± 0.002	1435.07	5.1	0.9544	0.7170
39	Eccq2...-0.25...-0.25...et0.1.D14	ET	2.	-0.25	-0.25	-0.25	14.0	0.068 ± 0.002	2001.7	5.6	0.9663	0.5261
40	Eccq2...0.25...0.25...et0.1.D14	ET	2.	0.25	0.25	0.25	14.0	0.103 ± 0.002	2707.25	8.3	0.9544	0.7155
41	Eccq2...-0.25...-0.25...et0.2.D14	ET	2.	-0.25	-0.25	-0.25	14.0	0.072 ± 0.001	1123.58	3.5	0.9660	0.5300
42	Eccq2...0.25...0.25...et0.2.D14	ET	2.	0.25	0.25	0.25	14.0	0.219 ± 0.002	1708.92	5.6	0.9548	0.7151
43	Eccq2...-0.25...-0.25...et0.2.D16	ET	2.	-0.25	-0.25	-0.25	16.0	0.225 ± 0.003	2085.67	5.8	0.9663	0.5253
44	Eccq2...0.25...0.25...et0.2.D16	ET	2.	0.25	0.25	0.25	16.0	0.188 ± 0.003	2847.34	8.3	0.9549	0.7165
45	Eccq2...-0.25...-0.25...et0.5.D26	ET	2.	-0.25	-0.25	-0.25	26.0	0.392 ± 0.003	3628.05	8.4	0.9665	0.5308
46	Eccq2...0.25...0.25...et0.5.D26	ET	2.	0.25	0.25	0.25	26.0	0.411 ± 0.004	5203.86	12.5	0.9542	0.7140
47	Eccq2...0.5...0.5...et0.1.D14	ET	2.	0.5	0.5	0.5	14.0	0.095 ± 0.002	2985.28	9.1	0.9448	0.8052
48	Eccq2...-0.5...-0.5...et0.1.D14	ET	2.	-0.5	-0.5	-0.5	14.0	0.158 ± 0.003	1714.88	4.2	0.9698	0.4279
49	Eccq2...-0.5...-0.5...et0.2.D16	ET	2.	-0.5	-0.5	-0.5	16.0	0.277 ± 0.003	1712.98	4.2	0.9696	0.4300
50	Eccq2...0.5...0.5...et0.2.D16	ET	2.	0.5	0.5	0.5	16.0	0.180 ± 0.003	3294.21	10.5	0.9451	0.8035
51	Eccq2...-0.5...-0.5...et0.5.D27	ET	2.	-0.5	-0.5	-0.5	27.0	0.393 ± 0.004	3522.66	7.2	0.9696	0.4328
52	Eccq2...-0.75...-0.75...et0.1.D14	ET	2.	-0.75	-0.75	-0.75	14.0	0.137 ± 0.002	1386.95	3.2	0.9725	0.3273
53	Eccq2...-0.75...-0.75...et0.2.D16	ET	2.	-0.75	-0.75	-0.75	16.0	0.125 ± 0.002	1353.72	3.4	0.9728	0.3297
54	Eccq3...0...0...et0.1.D13	ET	3.	0.	0.	0.	13.0	0.104 ± 0.002	1978.55	6.1	0.9713	0.5414
55	Eccq3...0...0...et0.2.D15	ET	3.	0.	0.	0.	15.0	0.166 ± 0.002	2156.21	6.2	0.9710	0.5401
56	Eccq3...0...0...et0.5.D26	ET	3.	0.	0.	0.	26.0	0.416 ± 0.004	5029.06	11.5	0.9710	0.5385
57	Eccq4...0...0...et0.1.D12	ET	4.	0.	0.	0.	12.0	0.134 ± 0.002	1609.06	5.3	0.9780	0.4725
58	Eccq4...0...0...et0.2.D15	ET	4.	0.	0.	0.	15.0	0.176 ± 0.002	2412.73	7.4	0.9779	0.4731
59	Eccq4...0...0...et0.5.D27	ET	4.	0.	0.	0.	27.0	0.412 ± 0.004	6698.64	15.2	0.9779	0.4739
60	Eccq4...0...0...et0.5.D27.5	ET	4.	0.	0.	0.	27.5	0.415 ± 0.005	7422.59	16.4	0.9784	0.4717

Table IV: Summary of the eccentric NR simulations used in this work. In the first column we indicate the identifier of the simulation. Additionally, each simulation is specified by its mass ratio $q = m_1/m_2 \geq 1$, the code with it was produced, the z-component of the dimensionless spin vectors, $\chi_{1,z}$, $\chi_{2,z}$, the orbital separation D/M and the initial orbital eccentricity, e_ω and its error, δe_ω , the time to merger, T_{merger}/M , the number of orbits, N_{orbits} , the final mass, M_f and the dimensionless final spin, χ_f .

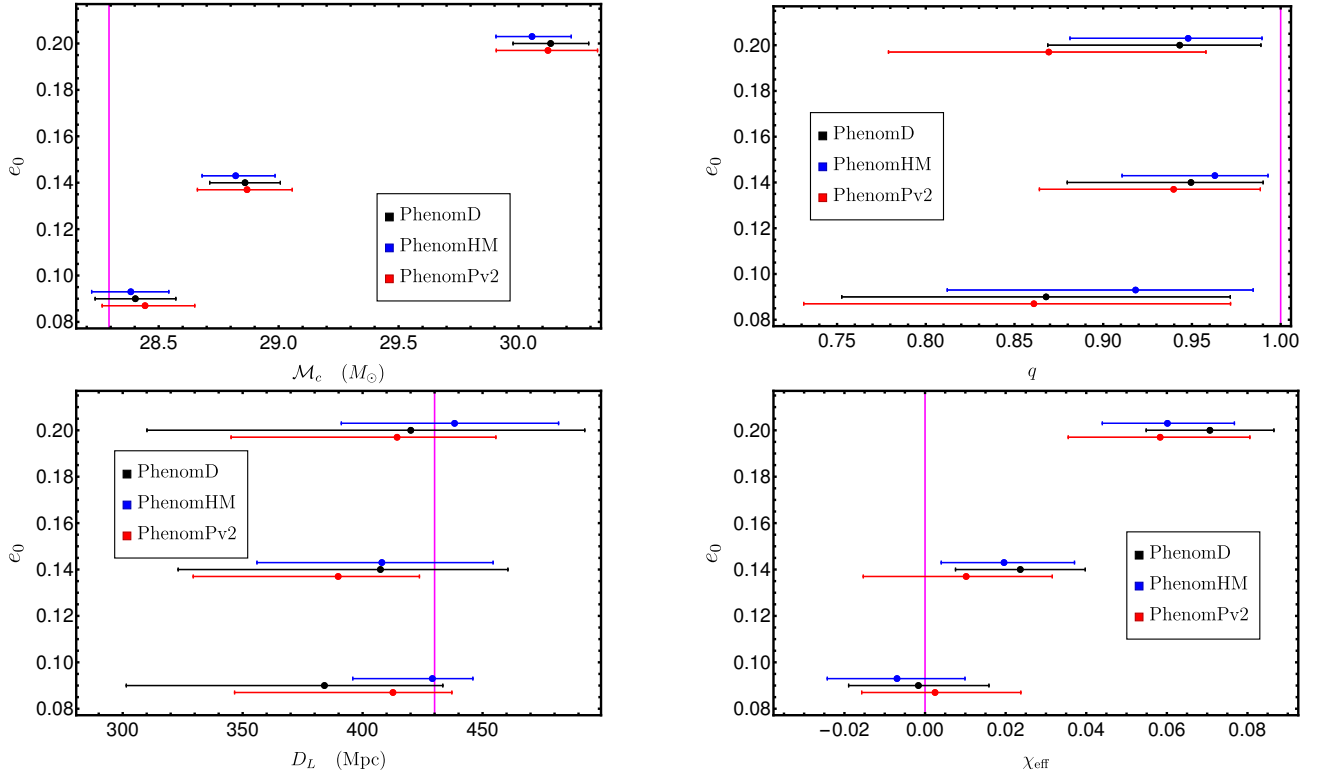


Figure 10: Median values and error bars corresponding to 90% credible regions of the posterior probability distributions for the injected NR simulations of Table I. The vertical magenta line represents the injected value. The black, blue and red segments represent the median values and errors bars of the distributions sampled using the IMRPhenomD, IMRPhenomHM and IMRPhenomPv2 approximants, respectively. The cases are represented for three initial eccentricities of the injected signal, $e_0 = 0.09, 0.14, 0.2$. To ease the visualization of the horizontal bars, cases with the same initial eccentricity and run with different approximants have been separated a $\Delta e = 0.003$.

-
- [1] B. P. Abbott *et al.* (LIGO Scientific Collaboration and Virgo Collaboration), *Phys. Rev. Lett.* **116**, 061102 (2016).
- [2] B. P. Abbott *et al.* (LIGO Scientific Collaboration and Virgo Collaboration), *Phys. Rev. Lett.* **116**, 241103 (2016).
- [3] B. P. Abbott *et al.* (VIRGO, LIGO Scientific), *Phys. Rev. Lett.* **118**, 221101 (2017), arXiv:1706.01812 [gr-qc].
- [4] B. P. Abbott *et al.* (Virgo, LIGO Scientific), *Astrophys. J.* **851**, L35 (2017), arXiv:1711.05578 [astro-ph.HE].
- [5] B. P. Abbott *et al.* (Virgo, LIGO Scientific), *Phys. Rev. Lett.* **119**, 141101 (2017).
- [6] B. P. Abbott *et al.* (Virgo, LIGO Scientific), *Phys. Rev. Lett.* **119**, 161101 (2017).
- [7] B. P. Abbott *et al.* (LIGO Scientific, Virgo), (2018), arXiv:1811.12907 [astro-ph.HE].
- [8] I. M. Romero-Shaw, P. D. Lasky, and E. Thrane, (2019), arXiv:1909.05466 [astro-ph.HE].
- [9] P. C. Peters and J. Mathews, *Phys. Rev.* **131**, 435 (1963).
- [10] P. C. Peters, *Phys. Rev.* **136**, B1224 (1964).
- [11] S. Husa, S. Khan, M. Hannam, M. Pürrer, F. Ohme, F. Jiménez Forteza, and A. Bohé, (2015).
- [12] S. Khan, S. Husa, M. Hannam, F. Ohme, M. Pürrer, X. Jiménez Forteza, and A. Bohé, *Phys. Rev. D* **93**, 044007 (2016), arXiv:1508.07253 [gr-qc].
- [13] M. Hannam, P. Schmidt, A. Bohé, L. Haegel, S. Husa, F. Ohme, G. Pratten, and M. Pürrer, *Phys. Rev. Lett.* **113**, 151101 (2014).
- [14] A. Bohé, L. Shao, A. Taracchini, A. Buonanno, S. Babak, I. W. Harry, I. Hinder, S. Ossokine, M. Pürrer, V. Raymond, T. Chu, H. Fong, P. Kumar, H. P. Pfeiffer, M. Boyle, D. A. Hemberger, L. E. Kidder, G. Lovelace, M. A. Scheel, and B. Szilágyi, *Phys. Rev. D* **95**, 044028 (2017).
- [15] L. London, S. Khan, E. Fauchon-Jones, C. García, M. Hannam, S. Husa, X. Jiménez-Forteza, C. Kalaghatgi, F. Ohme, and F. Pannarale, *Phys. Rev. Lett.* **120**, 161102 (2018).
- [16] R. Cotesta, A. Buonanno, A. Bohé, A. Taracchini, I. Hinder, and S. Ossokine, *Phys. Rev. D* **98**, 084028 (2018).
- [17] J. Blackman, S. E. Field, M. A. Scheel, C. R. Galley, D. A. Hemberger, P. Schmidt, and R. Smith, *Phys. Rev. D* **95**, 104023 (2017), arXiv:1701.00550 [gr-qc].
- [18] G. Pratten *et al.*, (2019).
- [19] C. García-Quirós *et al.*, (2019).
- [20] H. Estelles *et al.*, (2019).
- [21] K. Belczynski, D. E. Holz, T. Bulik, and R. O’Shaughnessy, *Nature* **534**, 512 (2016), arXiv:1602.04531 [astro-ph.HE].
- [22] D. Park, C. Kim, H. M. Lee, Y.-B. Bae, and K. Belczynski, *Mon. Not. Roy. Astron. Soc.* **469**, 4665 (2017), arXiv:1703.01568 [astro-ph.HE].

- [23] J. Samsing, Phys. Rev. D **97**, 103014 (2018).
- [24] J. Samsing, M. MacLeod, and E. Ramirez-Ruiz, Astrophys. J. **784**, 71 (2014), arXiv:1308.2964 [astro-ph.HE] .
- [25] T. Damour and N. Deruelle, Ann. Inst. Henri Poincaré Phys. Théor., Vol. 43, No. 1, p. 107 - 132 (1985).
- [26] T. Damour, A. Gopakumar, and B. R. Iyer, Phys. Rev. D **70**, 064028 (2004).
- [27] R.-M. Memmesheimer, A. Gopakumar, and G. Schäfer, Phys. Rev. D **70**, 104011 (2004).
- [28] S. Tanay, M. Haney, and A. Gopakumar, Phys. Rev. D **93**, 064031 (2016).
- [29] B. Moore, T. Robson, N. Loutrel, and N. Yunes, Class. Quant. Grav. **35**, 235006 (2018), arXiv:1807.07163 [gr-qc] .
- [30] N. Loutrel, S. Liebersbach, N. Yunes, and N. Cornish, Class. Quant. Grav. **36**, 025004 (2019), arXiv:1810.03521 [gr-qc] .
- [31] E. A. Huerta, C. J. Moore, P. Kumar, D. George, A. J. K. Chua, R. Haas, E. Wessel, D. Johnson, D. Glennon, A. Rebei, A. M. Holgado, J. R. Gair, and H. P. Pfeiffer, Phys. Rev. D **97**, 024031 (2018).
- [32] I. Hinder, L. E. Kidder, and H. P. Pfeiffer, Phys. Rev. D **98**, 044015 (2018).
- [33] Z. Cao and W.-B. Han, Phys. Rev. D **96**, 044028 (2017).
- [34] T. Hinderer and S. Babak, Phys. Rev. D **96**, 104048 (2017).
- [35] B. Brügmann, J. A. González, M. Hannam, S. Husa, U. Sperhake, and W. Tichy, Phys. Rev. D **77** (2008), 10.1103/physrevd.77.024027.
- [36] F. Löffler *et al.*, Class. Quant. Grav. **29**, 115001 (2012), arXiv:1111.3344 [gr-qc] .
- [37] I. Hinder, B. Vaishnav, F. Herrmann, D. M. Shoemaker, and P. Laguna, Phys. Rev. D **77**, 081502 (2008).
- [38] D. Pollney, C. Reisswig, E. Schnetter, N. Dorband, and P. Diener, Phys. Rev. D **83**, 044045 (2011).
- [39] A. Ramos-Buades, S. Husa, and G. Pratten, Phys. Rev. D **99**, 023003 (2019).
- [40] S. collaboration, “<https://www.black-holes.org/SpEC.html>,” .
- [41] J. Bowen and J. York, Phys. Rev. D **21**, 2047 (1980).
- [42] X. Jiménez-Forteza, D. Keitel, S. Husa, M. Hannam, S. Khan, and M. Pürrer, Phys. Rev. D **95**, 064024 (2017).
- [43] M. Campanelli, C. O. Lousto, Y. Zlochower, B. Krishnan, and D. Merritt, Phys. Rev. D **75**, 064030 (2007).
- [44] O. Dreyer, B. Krishnan, D. Shoemaker, and E. Schnetter, Phys. Rev. D **67**, 024018 (2003).
- [45] B. Bruegmann, J. A. Gonzalez, M. Hannam, S. Husa, U. Sperhake, and W. Tichy, Phys. Rev. D **77**, 024027 (2008), arXiv:gr-qc/0610128 [gr-qc] .
- [46] J. Thornburg, Phys. Rev. D **54**, 4899 (1996).
- [47] J. Thornburg, Class. Quant. Grav. **21**, 743 (2004), arXiv:gr-qc/0306056 [gr-qc] .
- [48] T. Mora and C. M. Will, Phys. Rev. D **66**, 101501 (2002).
- [49] S. Husa *et al.*, (2019).
- [50] M. Pürrer, S. Husa, and M. Hannam, Phys. Rev. D **85**, 124051 (2012), arXiv:1203.4258 [gr-qc] .
- [51] K. G. Arun, L. Blanchet, B. R. Iyer, and S. Sinha, Phys. Rev. D **80**, 124018 (2009).
- [52] A. Buonanno, Y. Chen, and T. Damour, Phys. Rev. D **74**, 104005 (2006).
- [53] C. K. Mishra, K. G. Arun, and B. R. Iyer, Phys. Rev. D **91**, 084040 (2015).
- [54] Y. Boetzel, C. K. Mishra, G. Faye, A. Gopakumar, and B. R. Iyer, (2019), arXiv:1904.11814 [gr-qc] .
- [55] J. C. Bustillo, A. Bohé, S. Husa, A. M. Sintes, M. Hannam, and M. Pürrer, (2015), arXiv:1501.00918 [gr-qc] .
- [56] L. Santamaría, F. Ohme, P. Ajith, B. Brügmann, N. Dorband, M. Hannam, S. Husa, P. Mösta, D. Pollney, C. Reisswig, and *et al.*, Phys. Rev. D **82** (2010), 10.1103/physrevd.82.064016.
- [57] I. MacDonald, S. Nissanke, and H. P. Pfeiffer, *Theory meets data analysis at comparable and extreme mass ratios. Proceedings, Conference, NRDA/CAPRA 2010, Waterloo, Canada, June 20-26, 2010*, Class. Quant. Grav. **28**, 134002 (2011), arXiv:1102.5128 [gr-qc] .
- [58] I. MacDonald, A. H. Mroué, H. P. Pfeiffer, M. Boyle, L. E. Kidder, M. A. Scheel, B. Szilágyi, and N. W. Taylor, Phys. Rev. D **87**, 024009 (2013).
- [59] M. Boyle, Phys. Rev. D **84**, 064013 (2011).
- [60] W. Tichy, B. Bruegmann, M. Campanelli, and P. Diener, Phys. Rev. D **67**, 064008 (2003).
- [61] N. Yunes and W. Tichy, Phys. Rev. D **74**, 064013 (2006).
- [62] N. Yunes, W. Tichy, B. J. Owen, and B. Bruegmann, Phys. Rev. D **74**, 104011 (2006).
- [63] C. Reisswig and D. Pollney, Class. Quant. Grav. **28**, 195015 (2011), arXiv:1006.1632 [gr-qc] .
- [64] LIGO Scientific Collaboration, (2018), 10.7935/GT1W-FZ16.
- [65] L. S. Finn and D. F. Chernoff, Phys. Rev. D **47**, 2198 (1993).
- [66] P. Jaranowski and A. Królak, Living Reviews in Relativity **15**, 4 (2012).
- [67] S. Husa, S. Khan, M. Hannam, M. Pürrer, F. Ohme, X. J. Forteza, and A. Bohé, Phys. Rev. D **93**, 044006 (2016).
- [68] “<https://dcc.ligo.org/LIGO-T0900288/public>.” .
- [69] D. A. Brown and P. J. Zimmerman, Phys. Rev. D **81**, 024007 (2010).
- [70] G. Ashton *et al.*, Astrophys. J. Suppl. **241**, 27 (2019), arXiv:1811.02042 [astro-ph.IM] .
- [71] J. Veitch and W. D. Pozzo, “CPNEST,” 10.5281/zenodo.322819 (2017).
- [72] C. R. Galley and P. Schmidt, (2016), arXiv:1611.07529 [gr-qc] .
- [73] P. Schmidt, I. W. Harry, and H. P. Pfeiffer, (2017), arXiv:1703.01076 [gr-qc] .
- [74] M. Favata, Phys. Rev. Lett. **112**, 101101 (2014).
- [75] E. A. Huerta, P. Kumar, S. T. McWilliams, R. O’Shaughnessy, and N. Yunes, Phys. Rev. D **90**, 084016 (2014).
- [76] I. Mandel, C. P. L. Berry, F. Ohme, S. Fairhurst, and W. M. Farr, Class. Quant. Grav. **31**, 155005 (2014), arXiv:1404.2382 [gr-qc] .
- [77] M. E. Lower, E. Thrane, P. D. Lasky, and R. Smith, Phys. Rev. D **98**, 083028 (2018).
- [78] J. Aasi *et al.* (LIGO Scientific), Class. Quant. Grav. **32**, 074001 (2015).
- [79] F. Acernese *et al.* (VIRGO), Class. Quant. Grav. **32**, 024001 (2015), arXiv:1408.3978 [gr-qc] .
- [80] S. Husa *et al.*, (2019).
- [81] P. Schmidt, F. Ohme, and M. Hannam, Phys. Rev. D **91**, 024043 (2015).